

${}^7\text{Li}$ NMR Study of Heavy Fermion LiV_2O_4 Containing Magnetic Defects

X. Zong, S. Das, F. Borsa,* M. D. Vannette, R. Prozorov, J. Schmalian, and D. C. Johnston
Ames Laboratory and Department of Physics and Astronomy, Iowa State University, Ames, Iowa 50011

(Dated: December 1, 2018)

We present a systematic study of the variations of the ${}^7\text{Li}$ NMR properties versus magnetic defect concentration n_{defect} within the spinel structure of polycrystalline powder samples ($n_{\text{defect}} = 0.21, 0.49,$ and 0.83 mol%) and a collection of small single crystals ($n_{\text{defect}} = 0.38$ mol%) of LiV_2O_4 in the temperature range from 0.5 to 4.2 K. We also report static magnetization measurements and ac magnetic susceptibility measurements at 14 MHz on the samples at low temperatures. Both the ${}^7\text{Li}$ NMR spectrum and nuclear spin-lattice relaxation rate are inhomogeneous in the presence of the magnetic defects. The ${}^7\text{Li}$ NMR data for the *powders* are well explained by assuming that (i) there is a random distribution of magnetic point defects, (ii) the same heavy Fermi liquid is present in the samples containing the magnetic defects as in magnetically pure LiV_2O_4 , and (iii) the influences of the magnetic defects and of the Fermi liquid on the magnetization and NMR properties are separable. In the *single crystals*, somewhat different behaviors are observed, possibly due to a modification of the heavy Fermi liquid, to a lack of separability of the relaxation effects due to the Fermi liquid and the magnetic defects, to non-Fermi liquid behavior of the conduction electrons, and/or to quantum fluctuations of finite-size magnetic defects (magnetic droplets). Remarkably, the magnetic defects in the powder samples show evidence of spin freezing below $T \approx 1.0$ K, whereas in the single crystals with similar magnetic defect concentration no spin freezing was found down to $T = 0.5$ K. Thus different types of magnetic defects and/or interactions between them appear to arise in the powders versus the crystals, possibly due to the substantially different synthesis conditions of the powders and crystals.

I. INTRODUCTION

LiV_2O_4 is a rare d -electron heavy fermion system at low temperatures $T < 10$ K.¹ The low temperature linear electronic specific heat coefficient γ (0.42 J/mol K²) and Pauli magnetic susceptibility χ_0 (≈ 0.01 cm³/mol) are 180 and 310 times those of a free electron gas, respectively, assuming each vanadium atom contributes 1.5 free electrons. The Wilson ratio R_W , which is the ratio of the enhancement factors of χ_0 and γ , is equal to 1.7, typical for a heavy fermion system.² Heavy fermion behavior was further confirmed by electrical resistivity measurements which show a T^2 dependence below 2 K with a large coefficient $A = 2.2$ $\mu\Omega$ cm/K².^{3,4} The A and γ values approximately follow the Kadowaki-Woods relation, $A/\gamma^2 = 1.0 \times 10^{-5}$ Ω cm/(mol K/J)², which holds for a variety of heavy fermion systems.⁵ Despite continuous theoretical work, a detailed explanation of the heavy fermion behaviors in LiV_2O_4 remains a challenge.^{6,7,8}

${}^7\text{Li}$ nuclear magnetic resonance (NMR) was an important local probe in establishing the low temperature heavy fermion behavior in magnetically pure samples of LiV_2O_4 .^{1,9} The low temperature ${}^7\text{Li}$ nuclear spin-lattice relaxation rate $1/T_1$ follows a Korringa relation $1/T_1 \propto T$, with a coefficient $1/T_1 T = 2.2$ s⁻¹K⁻¹, which is 6000 times larger than in the non-heavy fermion isostructural superconducting¹⁰ compound LiTi_2O_4 .¹¹ The Korringa ratio $\kappa = [4\pi k_B \gamma_n^2 / (\hbar \gamma_e^2)] K^2 T_1 T$, where K is the Knight shift, γ_n and γ_e are the gyromagnetic ratios of the ${}^7\text{Li}$ nuclear spin and the conduction electron spin, respectively, is equal to 0.7, which is close to the value of unity expected for a free electron gas.

Recently, we found that the low temperature ${}^7\text{Li}$

NMR properties of polycrystalline LiV_2O_4 are very sensitive to the presence of a small concentration of magnetic defects ($n_{\text{defect}} = 0.73$ mol%) within the spinel structure.^{12,13} In a sample containing a negligible concentration of magnetic defects, the longitudinal component of the global bulk ${}^7\text{Li}$ nuclear magnetization $M(t)$ after time delay t following a sequence of saturation pulses showed a single exponential recovery $1 - M(t)/M(\infty) = \exp[-(t/T_1)]$, where $1/T_1$ was proportional to T as noted above. However, in the sample with $n_{\text{defect}} = 0.73$ mol%, the $M(t)$ showed a stretched exponential recovery $1 - M(t)/M(\infty) = \exp[-(t/T_1^*)^\beta]$, with the characteristic relaxation rate $1/T_1^*$ showing a peak at $T \approx 0.7$ K. Here β is the stretching exponent with, in general, $0 < \beta < 1$. There was also a clear difference in the ${}^7\text{Li}$ NMR spectrum in these two samples. At low temperatures $T < 4.2$ K, the magnetically pure sample had a narrow spectrum with an almost temperature independent width (full width at half maximum peak intensity FWHM ~ 20 kHz). In contrast, a strong temperature dependent inhomogeneous broadening (FWHM ~ 100 kHz at $T < 4.2$ K) was observed in the sample with $n_{\text{defect}} = 0.73$ mol%.

In order to further clarify the nature of the magnetic defects and their effect on the heavy fermion properties of LiV_2O_4 , we report herein ${}^7\text{Li}$ NMR studies on LiV_2O_4 versus magnetic defect concentration. Three polycrystalline samples and a collection of single crystals are studied. The powder samples are labeled as 6b, 7a, and 6a, with $n_{\text{defect}} = 0.21$ mol%, 0.49 mol%, and 0.83 mol%, respectively. The single crystal sample is labeled as sample 1 with $n_{\text{defect}} = 0.38$ mol%. We determined the magnetic defect concentrations from static magnetization measurements in the temperature range 1.8–5 K and applied mag-

netic field range 0–5.5 T.¹⁴ Furthermore, to study the possible spin freezing of the magnetic defects at low temperatures, we measured the ac magnetic susceptibility at 14 MHz from 0.5 to 6 K of the single crystals and of the powder sample 6a with $n_{\text{defect}} = 0.83$ mol% using the tunnel-diode resonator technique.¹⁵

The temperature dependences of the ^7Li nuclear spin-lattice relaxation rates in our polycrystalline samples are similar to that of sample 3-3-a2 ($n_{\text{defect}} = 0.73$ mol%) that we studied in Ref. 12, which showed a peak in $1/T_1^*(T)$ at about 1 K. However, we find a qualitative difference in the temperature dependence of $1/T_1^*$ in the collection of single crystals, which instead decreases monotonically with decreasing temperature from 4.2 K down to 0.5 K. We include two important aspects into the analysis of the NMR data. First, we consider the effect of a distribution of local fields due to different positions of the ^7Li nuclei relative to their nearby magnetic defects. For the polycrystalline samples, this approach is quantitatively consistent with the inhomogeneous broadening of the spectrum and the nonexponential relaxation behavior. In the single crystals, this purely geometric origin for the nuclear relaxation fails to explain the observed behavior at $T \lesssim 1.3$ K. We then extend our analysis to take into account a possible size distribution of postulated magnetic defects of finite size (magnetic droplets). We speculate that the differences between the natures and interactions of the magnetic defects/droplets in the powders versus the crystals arise from the very different synthesis conditions and procedures of the powders and crystals.

The paper is organized as follows. Experimental details are given in Sec. II. In Sec. III, we report the experimental results of the magnetization, ac susceptibility, ^7Li NMR spectra, and ^7Li nuclear spin-lattice relaxation rate measurements. In Sec. IV, we analyze the NMR results. In Sec. V, we summarize the main conclusions of the paper.

II. EXPERIMENTAL DETAILS

Polycrystalline LiV_2O_4 samples were prepared using conventional solid state reaction at temperatures up to 700 °C. The starting materials were V_2O_3 (99.99%, MV Labs), V_2O_5 (99.99%, MV Labs), and Li_2CO_3 (99.999%, Alfa Aesar). Details of the sample synthesis procedure can be found in Ref. 14. The typical size of the polycrystalline grains is in the range of 1–10 μm ,¹⁶ as determined from scanning electron microscope (SEM) micrographs. Single crystals were grown at 950–1040 °C using a self-flux technique.¹⁷ The flux consisted of a mixture of Li_3VO_4 and LiV_2O_4 . The typical size of the crystals used in the present work is 0.2 mm. Static magnetization measurements were performed using a Quantum Design SQUID magnetometer in the temperature range 1.8–350 K and applied magnetic field range 0–5.5 T.

The ac magnetic susceptibility was measured using a

highly sensitive self-resonating LC circuit where losses are compensated by a tunnel diode that has a region of negative differential resistance in its I - V characteristic. The resonant frequency of an empty coil $f_0 = 1/(2\pi\sqrt{LC})$ changes when a sample is placed in the coil. The shift of the resonant frequency, $\Delta f = f(T, H) - f_0$ is directly related to the dimensionless volume ac susceptibility $\chi_{\text{ac}}(T, H)$ of the sample via¹⁵

$$\frac{\Delta f}{f_0} \approx -\frac{1}{2} \frac{V_s}{V_c} 4\pi\chi_{\text{ac}}, \quad (1)$$

where V_s is the sample volume and V_c is the coil volume. The volume magnetization is the magnetic moment per unit volume of the sample, with Gaussian units $\text{G cm}^3/\text{cm}^3 = \text{G}$. The volume susceptibility is the volume magnetization divided by field, which is then dimensionless. The optimized and thermally stabilized circuit resonates at 14 MHz with a stability of 0.05 Hz over hours.¹⁵ The resonator was mounted in a ^3He cryostat with a temperature range 0.5–150 K. A static external field up to 90 kOe can be applied to study field-dependent properties.

^7Li NMR measurements were performed utilizing a phase-coherent pulse spectrometer at applied magnetic fields $H = 1.06, 1.68$ and 3.0 T and in the temperature range 0.5–4.2 K. Measurements above 1.5 K were performed with a ^4He bath cryostat and measurements below 1.5 K with a Janis ^3He cryostat. The typical $\pi/2$ pulse length was 3 μs . The ^7Li NMR spectra for narrow lines (FWHM $\lesssim 100$ kHz) were measured by Fourier transform of half the Hahn echo signals, while for wider lines, the spectra were measured by integrating the echo area as a function of the applied magnetic field at a fixed frequency of rf pulses. Nuclear spin-lattice relaxation rates were measured by monitoring the recovery of the spin echo height using the standard saturation-recovery pulse sequence.

III. RESULTS

A. Magnetic Defect Concentrations

The magnetic defect concentrations of the samples were determined from the low temperature ($1.8 \text{ K} \leq T \leq 5 \text{ K}$) magnetization M versus applied magnetic field H isotherms.¹⁴ Figures 1(a), 1(b), 1(c), and 1(d) show the $M(H)$ isotherms at different temperatures for samples 6b, 1, 7a, and 6a, respectively. The magnetic defect concentration n_{defect} and spin value S of the magnetic defects in each sample are determined by fitting the equation

$$\begin{aligned} M(H, T) &= \chi_0 H + n_{\text{defect}} N_{\text{Ag}} g \mu_B S B_S(x) \\ &\equiv \chi_0 H + M_{\text{defect}}(H, T) \end{aligned} \quad (2)$$

to all the $M(H, T)$ isotherm data for each sample at $T \leq 5 \text{ K}$.¹⁴ In Eq. (2), n_{defect} is the magnetic defect concentration in dimensionless mole fraction units, χ_0

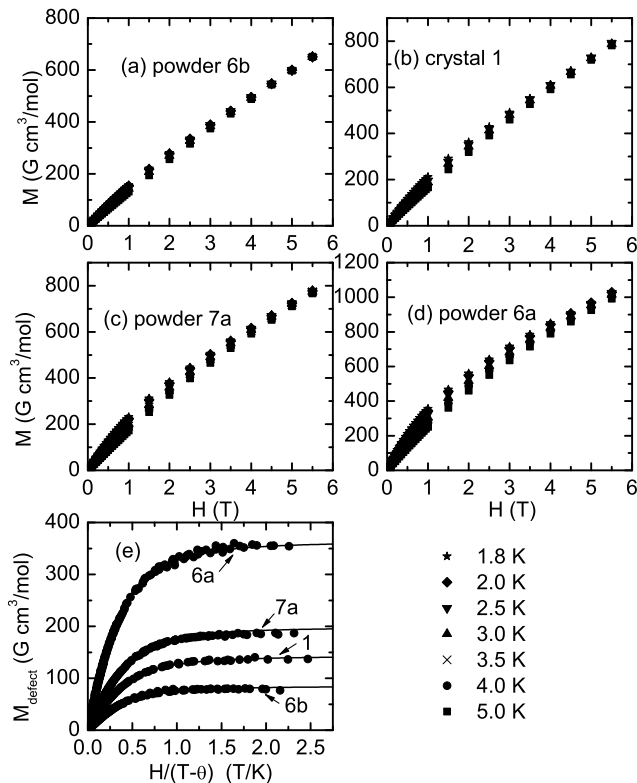


FIG. 1: (a)–(d) Magnetization M versus applied magnetic field H isotherms at different temperatures T for powder and crystals samples of LiV_2O_4 . (e) The magnetic defect contributions $M_{\text{defect}} = M - \chi_0 H$ to the data in panels (a)–(d) versus $H/(T - \theta)$. The χ_0 and θ values are listed in Table I. The solid lines are plots of the second term in Eq. (2), M_{defect} , versus $H/(T - \theta)$ with values of n_{defect} , θ , and S given in Table I.

is a field- and temperature-independent contribution to the molar susceptibility at low temperatures $T \leq 5$ K, N_A is Avogadro’s number, g is the (powder-averaged) spectroscopic splitting factor (g -factor) for the defect spins, $B_S(x)$ is the Brillouin function for spin S , and $x \equiv g\mu_B SH/[k_B(T - \theta)]$ where k_B is Boltzmann’s constant. We have replaced T in the usual Brillouin function by $(T - \theta)$ in order to take into account weak interactions between the magnetic defects. χ_0 , S , θ , and n_{defect} are free parameters in the fit, whereas the g value is fixed to be equal to 2 during the fit.¹⁴ The best fit parameters are listed in Table I. Figure 1(e) shows the magnetic defect magnetization contributions $M_{\text{defect}}(H, T) = M(H, T) - \chi_0 H$ versus $H/(T - \theta)$ for the four samples. All the data points in Figs. 1(a), 1(b), 1(c), and 1(d) fall onto a universal curve in Fig. 1(e) for each sample, respectively, as described by the second term in Eq. (2), thus confirming the consistency of the fits. The fitted functions $M_{\text{defect}}(H, T)$ in Eq. (2) for the four samples are plotted versus $H/(T - \theta)$ as the solid curves in Fig. 1(e) and show excellent agreement with the data.

TABLE I: Best fit values of the magnetic defect concentration n_{defect} , the spin value S , the intrinsic susceptibility χ_0 , and the effective Weiss temperature θ for powder samples 6b, 7a, and 6a and crystal sample 1 of LiV_2O_4 obtained by fitting Eq. (2) to the low temperature ($1.8 \text{ K} \leq T \leq 5 \text{ K}$) magnetization versus field isotherms in Figs. 1(a)–1(d) with $0 \leq H \leq 5.5 \text{ T}$.

Sample	n_{defect} (mol%)	S	χ_0 (cm^3/mol)	θ (K)
6b	0.21(1)	3.6(2)	0.0104(1)	−0.75(14)
7a	0.49(1)	3.5(1)	0.0108(1)	−0.57(6)
6a	0.83(3)	3.9(1)	0.0122(2)	−0.64(10)
1	0.38(1)	3.3(1)	0.01186(4)	−0.43(6)

Several features of the data in Table I are important. The low-temperature field-independent (up to 5.5 T) susceptibilities χ_0 of all four samples are the same to within about 10%, even though the magnetic defect concentrations change by a factor of 4, and are about the same as in magnetically pure LiV_2O_4 .^{1,14} This agreement suggests that the heavy Fermi liquid in magnetically pure LiV_2O_4 survives in the presence of the magnetic defects. Second, the spins S of the magnetic defects should be considered as average values, and these values are large, ranging from 3.3 to 3.9. That the magnetic defects have large spins is obvious from the data in Fig. 1(e) because the magnetic defect magnetizations are nearly saturated at relatively low fields of only ~ 2 T; spins 1/2 would not saturate even at our maximum field of 5.5 T. It is difficult to understand how such large spin values could arise from point defects in the crystal structure. In that case one might expect the magnetic defect spins to be much smaller and similar to those of V^{+4} ($S = 1/2$) or V^{+3} ($S = 1$). The large spins of the magnetic defects thus suggest that these spins may be associated with extended objects that we call “magnetic droplets” in Sec. IV C below instead of being associated with point-like local magnetic moments as in the usual picture. Third, the Weiss temperatures θ for all the samples are rather small, and indicate that the average interaction energy between the magnetic defects is also small and of order 1 K. Finally, from low-temperature magnetization measurements on many polycrystalline and single crystal samples that we have carried out in addition to those described here, the magnetic defect concentrations found do not exceed the largest value listed in Table I of 0.83 mol%.

B. ac Magnetic Susceptibility at 14 MHz

The ac magnetic susceptibility, $\chi_{\text{ac}} = dM/dH$, is an important parameter directly related to the electronic spin dynamics. It is very sensitive to collective behavior such as spin freezing and a transition to the glassy state. Figure 2 shows $\Delta\chi_{\text{ac}} \equiv \chi_{\text{ac}}(T) - \chi_{\text{ac}}(4.8 \text{ K})$ versus temperature T at various values of the external magnetic field for powder sample 6a with $n_{\text{defect}} = 0.83 \text{ mol\%}$.

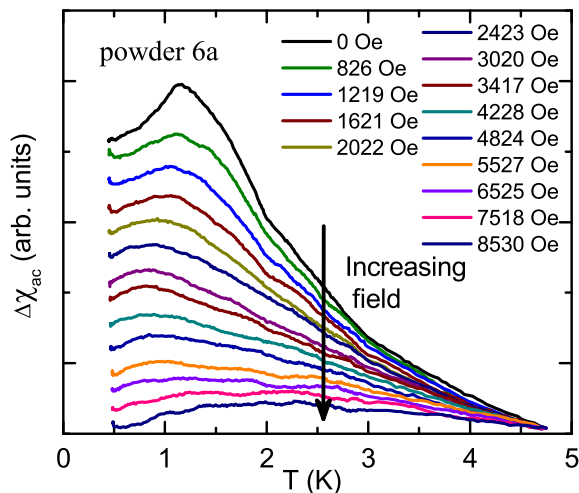


FIG. 2: (color online.) $\Delta\chi_{ac}$, the change of ac magnetic susceptibility χ_{ac} at 14 MHz relative to its value at 4.8 K, versus temperature T for LiV_2O_4 powder sample 6a with $n_{\text{defect}} = 0.83$ mol% at several values of the magnetic field (indicated in the legend). χ_{ac} decreases with increasing magnetic field.

Each curve corresponds to a magnetic field listed in the legend and the curves from top to bottom correspond to increasing magnetic field. We note that the change of the magnetic moment amplitude of the measured sample on decreasing the temperature from 1.1 K to 0.5 K in zero field corresponds to a change in magnetic moment of only about 5×10^{-10} G cm³, which cannot be resolved by a conventional SQUID magnetometer for the same size (~ 0.3 mm³) sample.

At zero static applied field, there is an obvious peak in $\Delta\chi_{ac}$ at about 1.1 K in Fig. 2 that is most likely indicative of a collective freezing of the magnetic moments. The field dependence of the magnetic susceptibility is characteristic of a spin glass system where spin randomness is suppressed by the uniaxial field and the peak in χ_{ac} associated with spin freezing is suppressed because the magnetic moments are closer to saturation. This result suggests collective freezing behavior of the magnetic defects in the LiV_2O_4 powder sample in zero field.

For our sample 1 consisting of a collection of single crystals with overall $n_{\text{defect}} = 0.38$ mol%, the situation is quite different. We cannot measure the spin susceptibility because the diamagnetic orbital susceptibility $\chi_{ac, \text{skin}}$ arising from skin depth effects dominates it. The skin depth δ can be calculated from¹⁸

$$\delta = \frac{504}{(\sigma K_m \nu)^{1/2}} \text{ meters}, \quad (3)$$

where K_m is relative permeability, σ is the conductivity in $\Omega^{-1}\text{m}^{-1}$, and ν is the applied frequency in Hz. Setting $K_m = 1$, $\sigma = 5 \times 10^6 \Omega^{-1}\text{m}^{-1}$ (σ value at 1.8 K in Ref. 17), and $\nu = 14$ MHz, we obtain $\delta \approx 0.06$ mm, significantly smaller than the size of a crystal in sample 1. Thus we expect that the $\chi_{ac, \text{skin}}$ contribution to

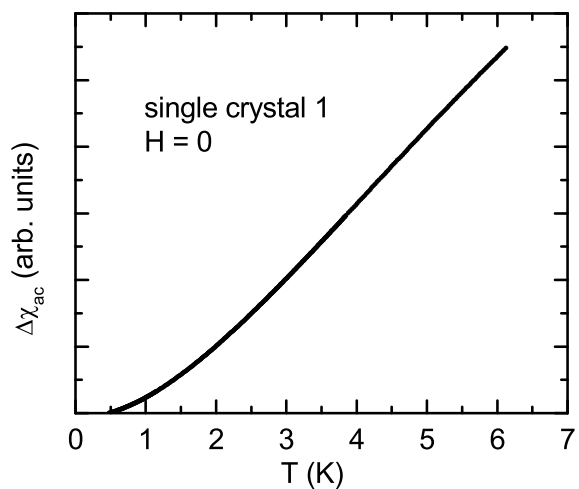


FIG. 3: $\Delta\chi_{ac}$, the change of ac magnetic susceptibility χ_{ac} relative to its value at 0.5 K, versus temperature T in single crystal LiV_2O_4 (sample 1) in zero applied magnetic field and at a frequency of 14 MHz.

χ_{ac} is significant and its effect increases with decreasing temperature as the resistivity decreases monotonically with decreasing temperature.^{3,4} Figure 3 shows the $\Delta\chi_{ac} \equiv \chi_{ac}(T) - \chi_{ac}(0.5 \text{ K})$ versus temperature T from 0.5 to 6 K. Since the static susceptibility of various samples is nearly T -independent or increases with decreasing T over this T range, the decrease in $\Delta\chi_{ac}$ with decreasing T in Fig. 3 indicates that $\chi_{ac, \text{skin}}(T)$ dominates the χ_{ac} response there. Furthermore, we see no evidence for a collective spin freezing for this sample, and we did not find any field dependence up to an applied field of 10 kOe (not shown). Thus, the measurement of the ac susceptibility at 14 MHz for our single crystals does not yield useful information for understanding the magnetic response of the magnetic defects in these crystals. $\chi_{ac}(H, T)$ measurements at much lower frequencies are called for.

C. ⁷Li NMR Line Width

The ⁷Li NMR absorption line width is related to the local static magnetic field distribution. It becomes broader with increasing concentrations of magnetic defects. Figure 4 shows the absorption lines of the four samples at temperature $T = 4.2$ K and $H = 1.06$ T. Although the ⁷Li nuclei have spin $I = 3/2$, both first and second order nuclear quadrupole broadening due to a structural distortion can be ruled out since we observe no satellite peaks or shortening of $\pi/2$ pulse length as compared to the magnetically pure LiV_2O_4 sample.^{19,20} The line width is significantly larger than the intrinsic width for an individual ⁷Li nuclear spin, indicating an inhomogeneous magnetic broadening of the line. The intrinsic line width is of the order of $1/T_2 \approx 5$ kHz, where T_2 is the nuclear spin-spin relaxation time and is almost indepen-

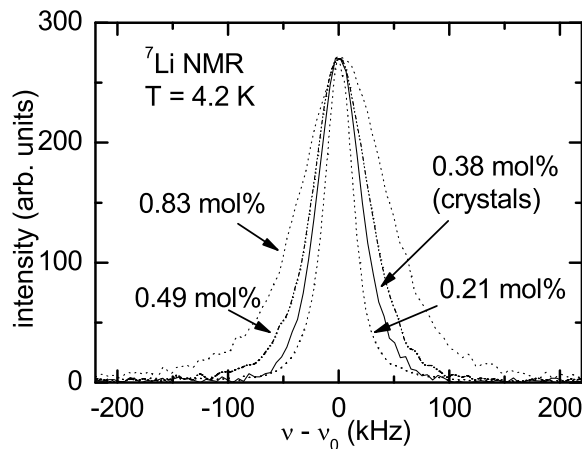


FIG. 4: The ${}^7\text{Li}$ NMR absorption versus rf frequency ν at temperature $T = 4.2$ K and applied magnetic field $H = 1.06$ T in the four LiV_2O_4 samples. The frequency $\nu_0 = 17.6$ MHz.

dent of the defect concentration and temperature below 4.2 K. Figure 5 displays the temperature dependences of the full width at half maximum peak intensity (FWHM) of the spectra for the four samples.

The broadening of the ${}^7\text{Li}$ NMR line has three contributions. The first contribution comes from the nuclear ${}^7\text{Li}$ - ${}^{51}\text{V}$ and ${}^7\text{Li}$ - ${}^7\text{Li}$ dipolar interactions. This contribution can be estimated using the Van Vleck second moment $\langle\Delta\omega^2\rangle$.²¹ A second broadening comes from the macroscopic field inhomogeneity due to a distribution of the demagnetization factors and a distribution of magnetic fields due to neighboring powder grains. This contribution is proportional to the magnetization of the sample and the resulting root mean square deviation of ${}^7\text{Li}$ NMR resonance frequencies can be written as $BM\rho_N\gamma_{\text{Li}}/2\pi$, where M is the molar susceptibility, ρ_N is the density of LiV_2O_4 formula units in the sample, γ_{Li} the gyromagnetic ratio of ${}^7\text{Li}$ nuclei, and B a dimensionless factor. B is estimated to be 1.43 for a close packed powder sample with ellipsoidal shapes.²² A third broadening contribution comes from inhomogeneity due to the presence of magnetic defects within the sample. An estimate for this contribution is not possible without a model of the nature of the defects and the types of interactions between the defects and nearby ${}^7\text{Li}$ nuclear spins. However, the presence of this contribution can be inferred by comparing the experimental FWHM values and the values expected when including only the first two contributions, as follows.

The FWHM resulting from the first two contributions can be calculated within a Gaussian approximation by

$$\text{FWHM}_a = 2.35\sqrt{\langle\Delta\omega^2\rangle/(2\pi)^2 + (BM\rho_N\gamma_{\text{Li}}/2\pi)^2} \quad (4)$$

with $B = 1.43$, and $\langle\Delta\omega^2\rangle^{1/2}/2\pi = 2.7$ kHz.²³ M is calculated from Eq. (2) using the parameter values listed in Table I. The FWHM_a calculated from Eq. (4) is plotted as the dashed lines in Fig. 5. It is clear that Eq. (4) cannot account for the observed broadening of the lines, so

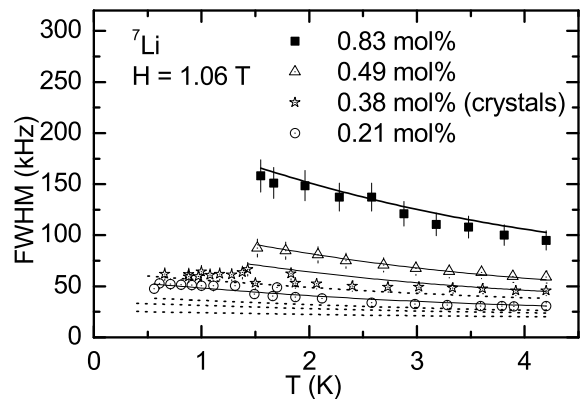


FIG. 5: Temperature T dependence of full width at half maximum peak intensity (FWHM) of the ${}^7\text{Li}$ NMR spectrum under external magnetic field $H = 1.06$ T in the four LiV_2O_4 samples. The symbols are experimental results. The dashed lines are plots of Eq. (4) (with $B = 1.43$) that takes into account the contributions due to powder broadening and nuclear dipole-dipole interactions, but does not take into account local field inhomogeneity due to the magnetic defects. The solid lines are fits by Eq. (7), which also takes into account the local field inhomogeneity. The fitted solid lines from bottom to top are for samples with $n_{\text{defect}} = 0.21, 0.38$ (crystals), 0.49, and 0.83 mol%, respectively.

a local magnetic field inhomogeneity due to the presence of the magnetic defects must be present in the samples. We will return to this issue in Sec. IV B 1.

D. Nuclear Spin-Lattice Relaxation Rates

The longitudinal ${}^7\text{Li}$ nuclear spin relaxation versus time $M(t)$ exhibits an increasingly nonexponential behavior with increasing concentration of magnetic defects or decreasing temperature. Figure 6 shows the recoveries of $M(t)$ following a saturation sequence for the four samples at different temperatures. The recovery data can be described by a stretched exponential function

$$1 - \frac{M(t)}{M(\infty)} = \exp[-(t/T_1^*)^\beta]. \quad (5)$$

The solid curves in Fig. 6 are best fits to the data by Eq. (5). The best fit values of $1/T_1^*(T)$ and $\beta(T)$ are shown in Figs. 7 and 8 for powder and single crystal samples, respectively.

The temperature dependence of $1/T_1^*$ is quite different in the powder and single crystal samples. A peak is observed in $1/T_1^*(T)$ for the powder samples 6a ($n_{\text{defect}} = 0.83$ mol%, $T_{\text{peak}} \approx 1.0$ K) and 7a ($n_{\text{defect}} = 0.49$ mol%, $T_{\text{peak}} \approx 0.6$ – 0.7 K). In the powder sample 6b with the smallest magnetic defect concentration ($n_{\text{defect}} = 0.21$ mol%), $1/T_1^*$ starts to increase at the lowest experimental temperatures and might exhibit a peak with further decreasing temperature. The peak positions in sample 6a for $H = 1.06$ and 1.68 T are almost the

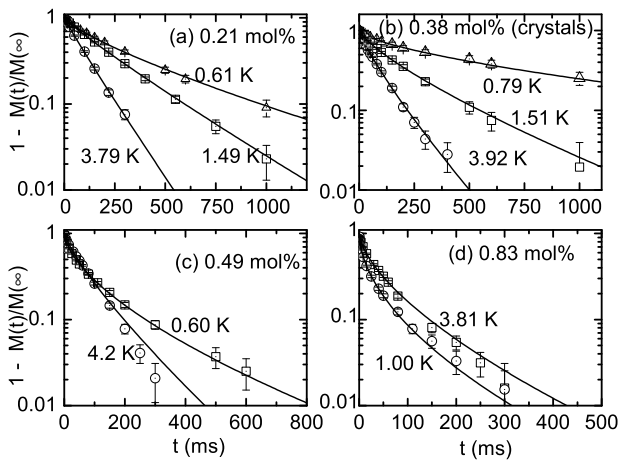


FIG. 6: Recovery of ${}^7\text{Li}$ nuclear magnetization $M(t)$ after time delay t following a sequence of saturation pulses. Note that M here is different from the electronic spin magnetization in Fig. 1. The data points were obtained in applied magnetic field $H = 1.06$ T at the indicated temperatures and with rf frequency $\nu = 17.6$ MHz for LiV_2O_4 samples with (a) 0.21 mol%, (b) 0.38 mol% (single crystals), (c) 0.49 mol%, and (d) 0.83 mol% magnetic defects. The solid curves are fits to the data by Eq. (5).

same as the peak position in $\chi_{\text{ac}}(T)$ for this sample at $H = 0$ in Fig. 2. We conclude that the peaks in $1/T_1^*$ originate from the spin freezing of the magnetic defects. In the crystal sample, $1/T_1^*(T)$ in Fig. 8 decreases monotonically with decreasing temperature with a $1/T_1^*$ value at 0.5 K much smaller than in the powder samples, and there is no sign of spin freezing.

Before ending this subsection, we comment about the effect of inhomogeneous broadening on the relaxation measurements. Because of the increasing inhomogeneous broadening with decreasing temperature, some of the ${}^7\text{Li}$ nuclei may be shifted out of the NMR spectrometer response window ($\Delta f \sim 200$ kHz) and excluded from the relaxation measurements. The number of observed ${}^7\text{Li}$ nuclei can be estimated from the product of fully recovered echo height $M(\infty)$ and the temperature, which is proportional to the nuclear Curie constant C in the Curie law for $M(\infty) = C/T$. These data are shown for $H = 1.06$ T versus temperature T in Fig. 9. For powder samples 6b ($n_{\text{defect}} = 0.21$ mol%) and 7a ($n_{\text{defect}} = 0.49$ mol%), the decrease of $M(\infty)T$ is less than 10% when the temperature decreases from 4.2 K to the lowest temperature (≈ 0.5 K). In contrast, for sample 6a ($n_{\text{defect}} = 0.83$ mol%), $M(\infty)T$ starts to decrease below $T \approx 3.5$ K and at the lowest temperature ($T \approx 0.5$ K), $M(\infty)T$ is about 50% of that at 4.2 K. As we will show below, the nuclei at the wings of the spectrum have an average relaxation rate larger than those at the center of the spectrum. Exclusion of those nuclei in sample 6a can thus result in a smaller measured relaxation rate in that sample.

In the single crystals, the normalized signal inten-

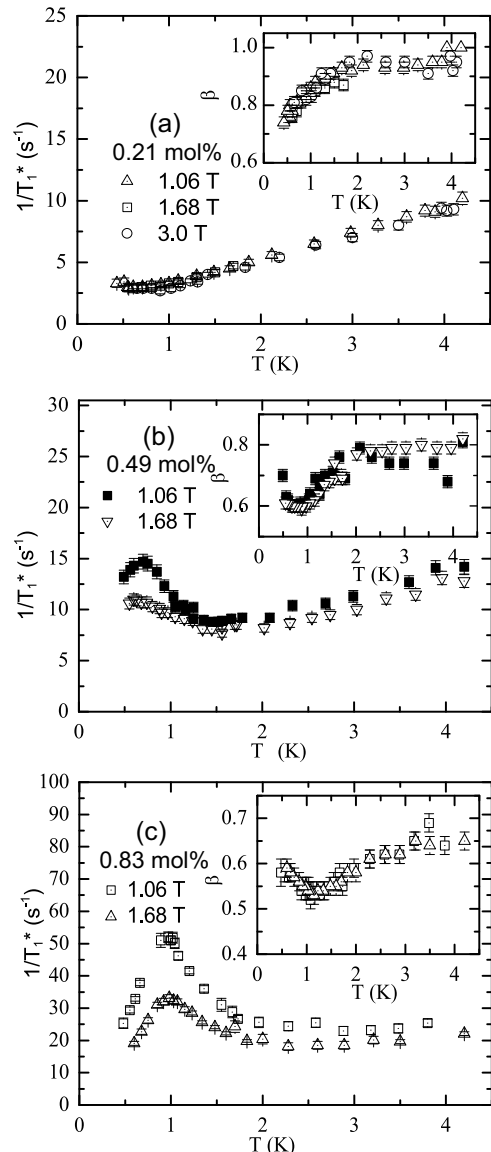


FIG. 7: $1/T_1^*$ and β versus temperature T of LiV_2O_4 obtained by fitting data as in Figs. 6(a), (c), and (d) by Eq. (5), of (a) powder sample 6b with $n_{\text{defect}} = 0.21$ mol% at external magnetic fields $H = 1.06$, 1.68, and 3.0 T, (b) powder sample 7a with $n_{\text{defect}} = 0.49$ mol% at $H = 1.06$, 1.68 T, and (c) powder sample 6a with $n_{\text{defect}} = 0.83$ mol% at $H = 1.06$ and 1.68 T.

sity $M(\infty)T$ also decreases with decreasing temperature. Since the line width in the crystals is less than in powder sample 7a (see Fig. 5), where no significant signal loss is observed, we attribute the signal loss to the effect of rf field skin depth. Here, only the ${}^7\text{Li}$ nuclear spins within the skin depth contribute to the NMR signal. Setting $K_m = 1$, $\sigma = 5 \times 10^6 \Omega^{-1}\text{m}^{-1}$ (the value of σ at 1.8 K in Ref. 17), and $\nu = 17.6$ MHz, Eq. (3) gives $\delta = 0.054$ mm, which is less than the typical size (0.2 mm) of the crystals. However, there is an unexplained kink in the data for the crystals at $T \approx 1.4$ K in both Figs. 8 and 9.

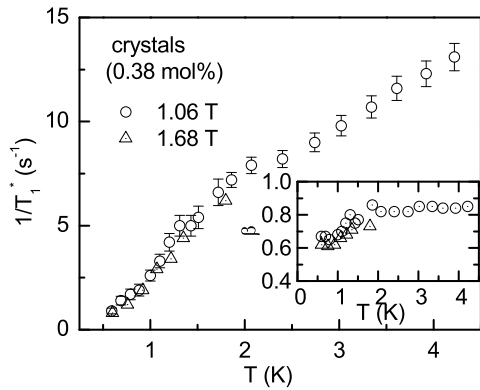


FIG. 8: $1/T_1^*$ and β versus temperature T of the LiV_2O_4 crystal sample 1 with $n_{\text{defect}} = 0.38$ mol% in external magnetic fields $H = 1.06$ and 1.68 T, obtained by fitting data as in Fig. 6(b) by Eq. (5).

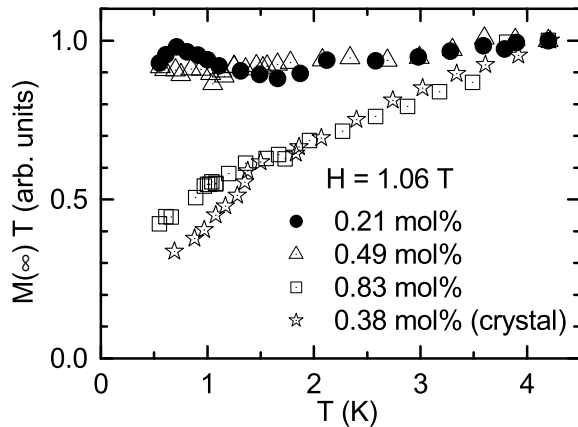


FIG. 9: The fully recovered echo intensity $M(\infty)$, which is the total equilibrium nuclear magnetization, times temperature T in the nuclear spin-lattice relaxation rate measurements of the four LiV_2O_4 samples in an applied field $H = 1.06$ T.

E. Relaxation at Different Positions in the Spectra

The observation of a stretched exponential relaxation behavior indicates the presence of a distribution of nuclear spin-lattice relaxation rates $1/T_1$. In order to study the origin of the $1/T_1$ distribution, we performed the following “hole burning” experiment. This experiment extends our previous hole burning experiment briefly described in Ref. 12. We also studied the relaxation behavior at different positions of the NMR absorption line.

Figures 10(a) and (b) display the recovery of a “hole” in the echo spectrum in applied magnetic field $H = 1.06$ T, obtained from Fourier transform of half the Hahn echo signal generated by two strong rf pulses following a weak $\pi/2$ pulse in samples 6a ($n_{\text{defect}} = 0.83$ mol%) and 6b ($n_{\text{defect}} = 0.21$ mol%), respectively. The weak $\pi/2$ pulse has a width of $56 \mu\text{s}$ and most of its power is distributed within a narrow frequency window of width

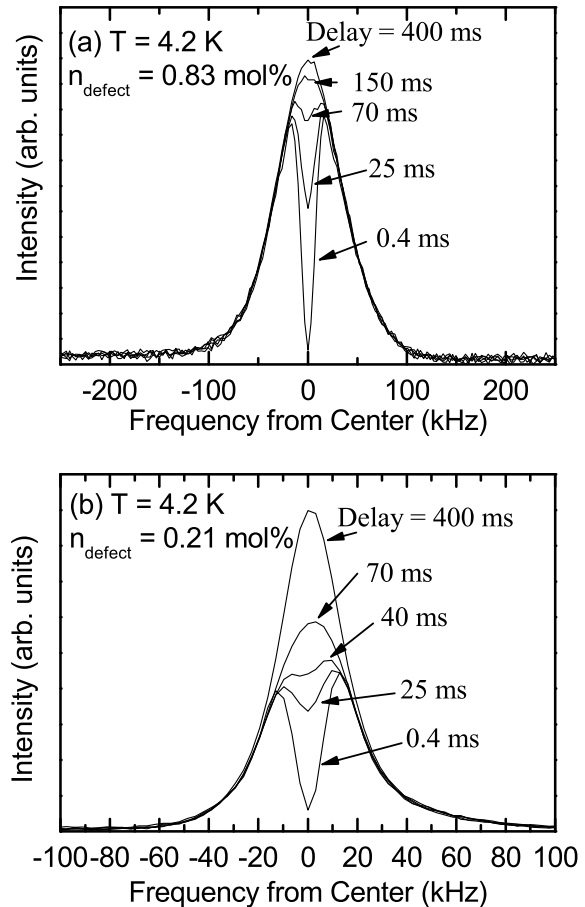


FIG. 10: Recovery at 4.2 K of a “hole” in the absorption spectrum of LiV_2O_4 produced by a weak $\pi/2$ pulse with pulse length of $56 \mu\text{s}$ at delay = 0 in sample (a) 6a ($n_{\text{defect}} = 0.83$ mol%) and (b) 6b ($n_{\text{defect}} = 0.21$ mol%). The applied magnetic field H is 1.06 T and the center frequency is 17.6 MHz. The delay times after which the spectra were measured by two strong rf pulses are given in the figures. Note the different abscissa scales in (a) and (b).

≈ 40 kHz. Such a weak $\pi/2$ pulse only saturates the central part of the spectrum. It is clear that the hole recovery process does not affect the rest of the line and thus spectral diffusion does not occur in our time scale. That is, nuclei with different Larmor frequencies are not coupled to each other over the NMR relaxation time scale of $T_1 \sim 100$ ms.

Lack of spectral diffusion as observed above allows us to investigate the nuclear spin-lattice relaxation at different positions of the spectrum. Due to the strong ${}^7\text{Li}$ NMR signal at low temperatures, we were able to study the relaxation of ${}^7\text{Li}$ far out on the wings of the spectrum although the signal intensity is much weaker than at the peak. Figure 11 displays the nuclear spin-lattice relaxation curves of powder sample 7a ($n_{\text{defect}} = 0.49$ mol%) in $H = 1.68$ T with the rf pulse frequency equal to, 400 kHz higher than, or 400 kHz lower than, the peak frequency of the line. All three recovery curves are nonexponen-

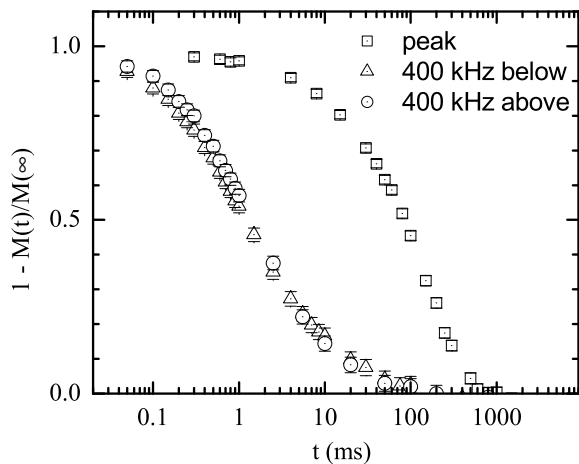


FIG. 11: Recovery at 4.2 K of ${}^7\text{Li}$ longitudinal nuclear magnetization $M(t)$ following a saturation sequence at time $t = 0$ measured at different positions of the spectrum in LiV_2O_4 powder sample 7a ($n_{\text{defect}} = 0.49$ mol%) under external magnetic field $H = 1.68$ T. The recovery curves, which are non-exponential, were measured with rf pulse frequency (\square) equal to the peak of the spectrum (27.8 MHz) and at $T = 1.56$ K, (\triangle) 400 kHz lower than the peak and at $T = 1.53$ K, and (\circ) 400 kHz higher than the peak and at $T = 1.77$ K, respectively.

tial. It is clear from Fig. 11 that the nuclei close to the peak of the line have an average relaxation rate lower than those away from the peak. As will be discussed below, the behavior in Fig. 11 is consistent with an inhomogeneous local magnetic field induced by the magnetic defects. It is noted that the temperatures at which the three relaxation curves were taken are slightly different. However, such small temperature differences should be negligible compared to the large difference of relaxation rates between these three curves.

IV. ANALYSIS

A. Introduction

A model for the microscopic nature of the magnetic defects has to be assumed in order to analyze the NMR results. We will examine two related possibilities. First, in Sec. IV B we treat the magnetic defects as traditional identical localized magnetic moments. The distribution of ${}^7\text{Li}$ nuclear spin-lattice relaxation rates and the inhomogeneous broadening of the ${}^7\text{Li}$ absorption spectrum are then entirely caused by the local field inhomogeneity, which arises from a distribution of positions of the ${}^7\text{Li}$ nuclei relative to the magnetic defects. In a refined version of this model in Sec. IV C, the magnetic defects are assumed to actually be “magnetic droplets” that have a distribution of sizes. In this refined approach, the distribution of the dynamic properties of the droplets also needs to be considered.

We will assume at the outset that the heavy Fermi liquid present in magnetically pure LiV_2O_4 is not affected by the presence of the magnetic defects. The measured ${}^7\text{Li}$ relaxation versus time following saturation then arises from two mechanisms. The first is a single-exponential relaxation that is the same as in magnetically pure LiV_2O_4 and that comes from the contact interaction of ${}^7\text{Li}$ nuclear spins with the conduction electron spins in the heavy Fermi liquid. The second mechanism is the hyperfine interaction of the nuclei with the magnetic defects. The first (homogeneous) mechanism gives a relaxation rate described by the Korringa law with $1/T_1 \propto T$.²⁴ The main goal of the present modeling is to then determine the (second) contribution of the magnetic defects to the time-dependent nuclear relaxation and to subsequently interpret what that contribution means. The separation of these two contributions to the magnetic properties, at least above 1.8 K, is supported by previous magnetization measurements^{1,14} as well as by those in Sec. III A above. The magnetization as expressed in Eq. (2) contains a contribution $\chi_0 H$ almost independent of the magnetic defect concentration (see Table I). This contribution is most likely due to the same heavy Fermi liquid that is present in magnetically pure LiV_2O_4 at low temperatures.

We will see that this separation of the magnetic properties into a heavy Fermi liquid part and a magnetic defect part can consistently explain our ${}^7\text{Li}$ NMR measurements on our powder samples of LiV_2O_4 . However, as we will show in Fig. 13(a) below, our NMR longitudinal magnetization recovery data below ~ 1.3 K for our sample of *single crystals* indicate that the Fermi liquid is modified by the presence of magnetic defects and/or that our model for the magnetic defects is no longer accurate below that temperature in our single crystals. This differentiation between the bulk crystal and powder properties indicates that there are differences between the natures of the magnetic defects and/or their interactions in single crystals as compared to powders, which in turn are likely associated in some way with the quite different preparation conditions of the two types of samples.

B. Geometric Inhomogeneity

1. ${}^7\text{Li}$ NMR Line Width

First we will analyze the ${}^7\text{Li}$ NMR line width by considering the distribution of distances between nuclear spins and point-like magnetic defects within the spinel structure. Dilute paramagnetic centers give rise to a broadening of the NMR spectrum through inhomogeneous dipolar and RKKY interactions and in the limit of great dilution the line shape approaches a Lorentzian with full

width at half maximum intensity (FWHM_b) given by²⁵

$$\begin{aligned} \text{FWHM}_b &= An_{\text{defect}} \frac{8\pi\rho_N}{9\sqrt{3}} g\mu_B\gamma_{\text{Li}} \langle S_z \rangle \\ &= 4.5An_{\text{defect}} SB_S(x) \text{ MHz}, \end{aligned} \quad (6)$$

where $\rho_N = 1.44 \times 10^{22} \text{ cm}^{-3}$ is the number density of LiV_2O_4 formula units, $A = 1$ for purely dipolar interactions and $A > 1$ if the RKKY interaction is also important, $\langle S_z \rangle$ is the thermal average value of magnetic defect spin polarization along the direction of the applied magnetic field and is equal to $SB_S(x)$ with $x = g\mu_B SH/[k_B(T - \theta)]$ [see Eq. (2)]. The line shape due to the dilute magnetic defects is Lorentzian²⁵ while the line shape due to the two contributions in Eq. (4) is Gaussian.^{21,22} In order to obtain the final FWHM value, we convolute a Gaussian distribution with FWHM = 1 with a Lorentzian distribution that has FWHM = x and the same mean value as the Gaussian distribution. We find that the FWHM of the convoluted distribution can be approximated by $(1 + x^{8/5})^{5/8}$ to within 10% for all values of x . We estimate the total FWHM by combining Eqs. (4) and (6) according to

$$\begin{aligned} \text{FWHM} &= (\text{FWHM}_a^{8/5} + \text{FWHM}_b^{8/5})^{5/8} \\ &= \left\{ \text{FWHM}_a^{8/5} + [4.5An_{\text{defect}} SB_S(x) \text{ MHz}]^{8/5} \right\}^{5/8}. \end{aligned} \quad (7)$$

Using the values of n_{defect} , S and θ in Table I and the results for FWHM_a in Fig. 5, the FWHM data in Fig. 5 for all four samples were simultaneously fitted by Eq. (7), except for the single crystal data below 1.3 K, where the nuclear spin-lattice relaxation rates in Fig. 8 indicate a possible screening of the magnetic defects. The only fitting parameter was A , and the best fit value was $A = 1.4$. The best fit to the data is displayed as the set of solid curves in Fig. 5. The high quality of the fit shows that the local field inhomogeneity at the ${}^7\text{Li}$ nuclear sites arising from the distribution of distances between the ${}^7\text{Li}$ nuclei and the magnetic defects is an essential contributor to the ${}^7\text{Li}$ NMR line width.

2. ${}^7\text{Li}$ Nuclear Spin-Lattice Relaxation

In the present approach we treat the magnetic defects as identical localized magnetic moments. The distribution of ${}^7\text{Li}$ nuclear spin-lattice relaxation rates $1/T_1$ then arises from a distribution of fluctuating local magnetic fields at the nuclear sites due to a distribution in the positions of the nuclei relative to the magnetic defects. Since the relative positions of the ${}^7\text{Li}$ nuclei with respect to the magnetic defects are fixed, the shape of the ${}^7\text{Li}$ $1/T_1$ probability distribution due to the defects should be temperature independent. This would give rise to a temperature independent β value^{12,26} in the stretched exponential function in Eq. (5) if there were no additional contributions to the ${}^7\text{Li}$ nuclear spin-lattice relaxation.

The observed temperature dependences of the stretching exponent β in the insets of Figs. 7 and 8 are explained in this model by the additional Korringa contribution to $1/T_1$ that is proportional to the temperature. Since the nuclear spin-lattice relaxation rate due to itinerant conduction electrons is assumed to be homogeneous across the sample since it results from the contact interaction between the nuclear and conduction electron spins, the nuclear spin recovery due to the conduction electrons alone should be a single exponential. As just discussed, the recovery due to the magnetic defects alone should be a stretched exponential function with a temperature-independent β . The observed temperature dependent β arises in our model from different temperature dependences of the Korringa and magnetic defect contributions to the nuclear spin-lattice relaxation. Different temperature dependences result in different weights of these two contributions at different temperatures and accordingly different β values are seen at different temperatures when the total recovery is fitted by a stretched exponential function Eq. (5). Similarly, it is not appropriate to analyze the $1/T_1^*(T)$ data in Figs. 7 and 8 in terms of a sum of contributions from the heavy Fermi liquid and from the local magnetic defects, because their respective contributions to $1/T_1^*(T)$ cannot be deconvoluted.

To determine the magnetic defect contribution to the ${}^7\text{Li}$ nuclear spin dynamics, we first extract from the observed ${}^7\text{Li}$ nuclear spin-lattice relaxation versus time $M(t)$ data what the contribution of the magnetic defects is, and *then* derive parameters describing the relaxation by the magnetic defects. To accomplish the former goal, we write $1 - M(t)/M(\infty) = p(t) \exp(-t/T_{1K})$, where $p(t)$ is the contribution to the ${}^7\text{Li}$ nuclear spin relaxation from the magnetic defects and $\exp(-t/T_{1K})$ is the Korringa contribution from the heavy Fermi liquid, where we assume a concentration independent Korringa relaxation rate $1/T_{1K} = (2.2 \text{ s}^{-1}\text{K}^{-1})T$ and the coefficient of T is taken to be the value in a magnetically pure sample.¹² Then one obtains

$$p(t) = \left[1 - \frac{M(t)}{M(\infty)} \right] \exp\left(\frac{t}{T_{1K}}\right). \quad (8)$$

Thus $p(t)$ is determined by multiplying the experimentally observed $1 - M(t)/M(\infty)$ by $\exp(t/T_{1K})$.

We find that the magnetic defect contribution $p(t)$ to the ${}^7\text{Li}$ nuclear spin-lattice relaxation usually follows a stretched exponential time dependence in our temperature range $0.5 \leq T \leq 4.2 \text{ K}$ with a temperature- and magnetic defect concentration-independent stretching exponent β , as anticipated above, where we find that β has the specific value $\beta = 1/2$. Thus we obtain

$$p(t) = \exp[-(t/T_{1d}^*)^{1/2}], \quad (9)$$

where the new parameter T_{1d}^* takes the place of T_1^* in Eq. (5). Figures 12 and 13(a) show plots of the logarithm of $p(t)$ versus $t^{1/2}$ in external magnetic field $H = 1.06 \text{ T}$ and at different temperatures for powder

and single crystal samples, respectively. In powder samples 7a ($n_{\text{defect}} = 0.49$ mol%) and 6a ($n_{\text{defect}} = 0.83$ mol%), $p(t)$ can be fitted very well by Eq. (9) at all temperatures, as shown by the linear fits in Figs. 12(b) and (c), respectively. In powder sample 6b with a smaller $n_{\text{defect}} = 0.21$ mol% in Fig. 12(a), $p(t)$ follows root exponential behavior for all times t at the higher temperatures but only at short times at the low temperature of 0.61 K. We infer in Sec. IV B 4 below that the deviation at longer times is due to the effect of spin diffusion. In the crystals, $p(t)$ in Fig. 13(a) follows root exponential decay above 1.3 K but at lower temperature $p(t)$ instead shows an unphysical increase at later times. This unphysical behavior suggests that Eq. (8) overestimates the conduction electron contribution to the nuclear spin-lattice relaxation at temperatures below 1.3 K, the separability of the relaxation due to the magnetic defects from that due to the conduction electrons is no longer appropriate in that temperature regime, or the conduction electrons no longer form a Fermi liquid. An additional possible reason for the unphysical behavior is given in Sec. IV C. Resolving this issue is an important topic for future research.

We extract $1/T_{1d}^*$ versus temperature from the slopes of the fitted lines of $\log[p(t)]$ versus $t^{1/2}$ in Figs. 12 and 13(a) according to Eq. (9). The results are displayed in Figs. 13(b) and 14 for the single crystal and powder samples, respectively. The $1/T_{1d}^*$ versus T in powder samples 7a and 6a in Figs. 14(b) and (c), respectively, show an almost field independent peak, similar to the peaks in $1/T_1^*$ versus T in Figs. 7(b) and (c). As discussed above, the peaks are attributed to spin freezing of the magnetic defects. For the single crystals, we only extract $1/T_{1d}^*$ values above 1.3 K for reasons discussed above. Here $1/T_{1d}^*$ is nearly constant from 4.2 K down to about 2 K, but then shows a decrease upon further decrease in T . This behavior is very different from that of the powders.

The above root exponential relaxation behavior has been reported previously in systems where the nuclear spin-lattice relaxation rate is proportional to $1/r^6$, where r is the distance between a nucleus and a nearby paramagnetic center, and no nuclear spin diffusion takes place.^{27,28} Nuclear spin-lattice relaxation due to fluctuations of both dipolar and RKKY interactions have such $1/r^6$ dependences. In general, one can write the nuclear spin-lattice relaxation rate at the nuclear site \mathbf{r} due to a nearby paramagnetic center at location \mathbf{R}_l as

$$\frac{1}{T_1(\mathbf{r}, \mathbf{R}_l)} = C_l \frac{f(\theta)}{\bar{f}} \frac{1}{|\mathbf{r} - \mathbf{R}_l|^6}, \quad (10)$$

where $\mathbf{r} - \mathbf{R}_l$ is the vector connecting the paramagnetic center and nuclear spin, θ is the angle between $\mathbf{r} - \mathbf{R}_l$ and the external magnetic field, $f(\theta)$ is the angular dependence of $1/T_1(\mathbf{r}, \mathbf{R}_l)$, \bar{f} is the average of $f(\theta)$ over all directions, and

$$C_l = C_0 \frac{\tau_l}{1 + (\omega_n \tau_l)^2} \quad (11)$$

is a parameter proportional to the spectral density of spin

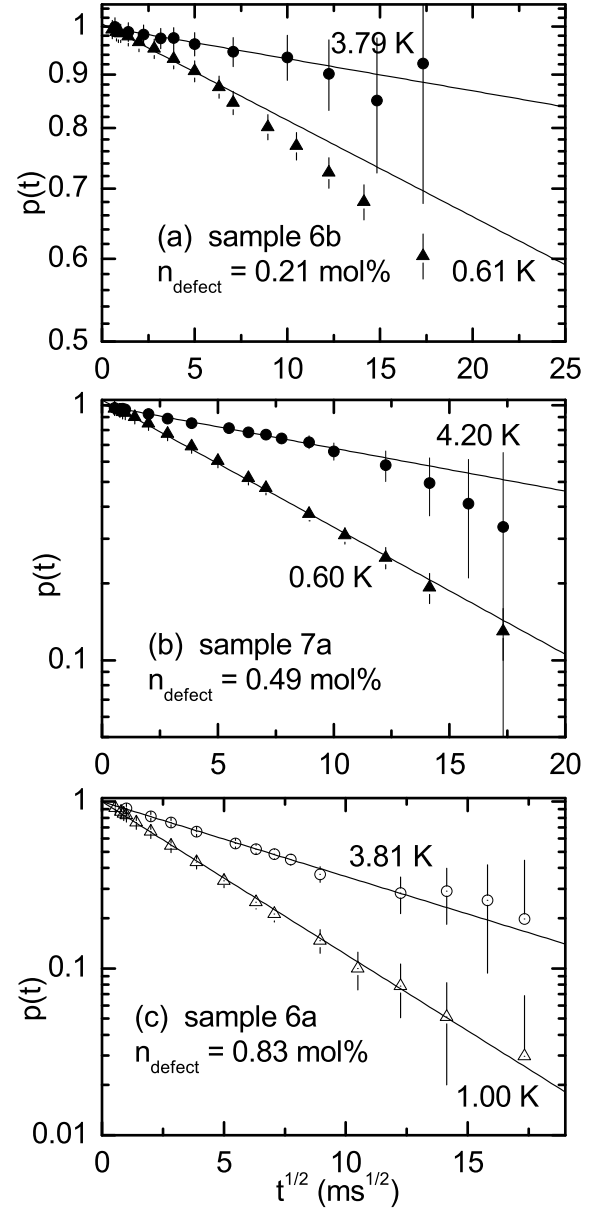


FIG. 12: Semilog plot of $p(t)$ in Eq. (8) versus the square root of the delay time $t^{1/2}$ for the LiV_2O_4 powder samples (a) 6b with $n_{\text{defect}} = 0.21$ mol%, (b) 7a with $n_{\text{defect}} = 0.49$ mol%, and (c) 6a with $n_{\text{defect}} = 0.83$ mol% at applied magnetic field $H = 1.06$ T and different temperatures. The straight lines are best fits of the data by Eq. (9), with parameters $1/T_{1d}^*$ given in Fig. 14.

fluctuations (with correlation time τ_l) at the nuclear Larmor frequency ω_n .²⁷ The defect contribution of the recovery of the nuclear magnetization towards equilibrium is then given as

$$p(\mathbf{r}, t) = \exp \left[-t \sum_l \frac{1}{T_1(\mathbf{r}, \mathbf{R}_l)} \right], \quad (12)$$

where the sum is over all defect sites. We first ignore the spatial variation of the microscopic relaxation rate, i.e.

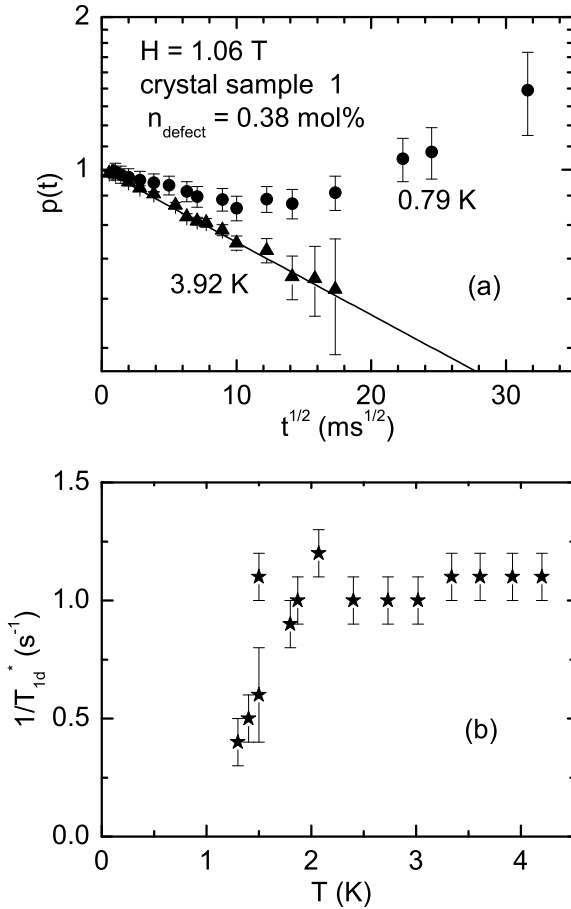


FIG. 13: (a) Semilog plot of the relaxation function $p(t)$ in Eq. (8) versus the square root of the delay time $t^{1/2}$ for the LiV_2O_4 crystal sample 1 with $n_{\text{defect}} = 0.38$ mol% at applied magnetic field $H = 1.06$ T and at two different temperatures. The upturn in the 0.79 K data at large times is unphysical (see text). The straight line is a best fit of the 3.92 K data by Eq. (9). (b) $1/T_{1d}^*$ in Eq. (9) versus temperature T in $H = 1.06$ T and above 1.3 K, where the upturn seen for $T = 0.79$ K in (a) is absent.

we assume that $\tau_l = \tau$ is the same for all defects, and concentrate on the geometric inhomogeneity as caused by a varying distance between nuclear spins and defects. In order to evaluate the average over defect positions we write $\sum_l h(\mathbf{R}_l) = \sum_i g_i h(\mathbf{x}_i)$ where $h(\mathbf{y}_i)$ is an arbitrary function of position \mathbf{y}_i , \mathbf{x}_i is a vanadium site position, we assume the magnetic defects are at vanadium lattice sites, and the sum over i now runs over all vanadium sites, not only magnetic defect sites. The random variable g_i is 1 with probability n_{defect} and 0 with probability $(1 - n_{\text{defect}})$ and assumed uncorrelated for different sites, i.e. defect positions are uncorrelated. Following Refs. 27 and 28 we obtain in the limit of low defect concentration

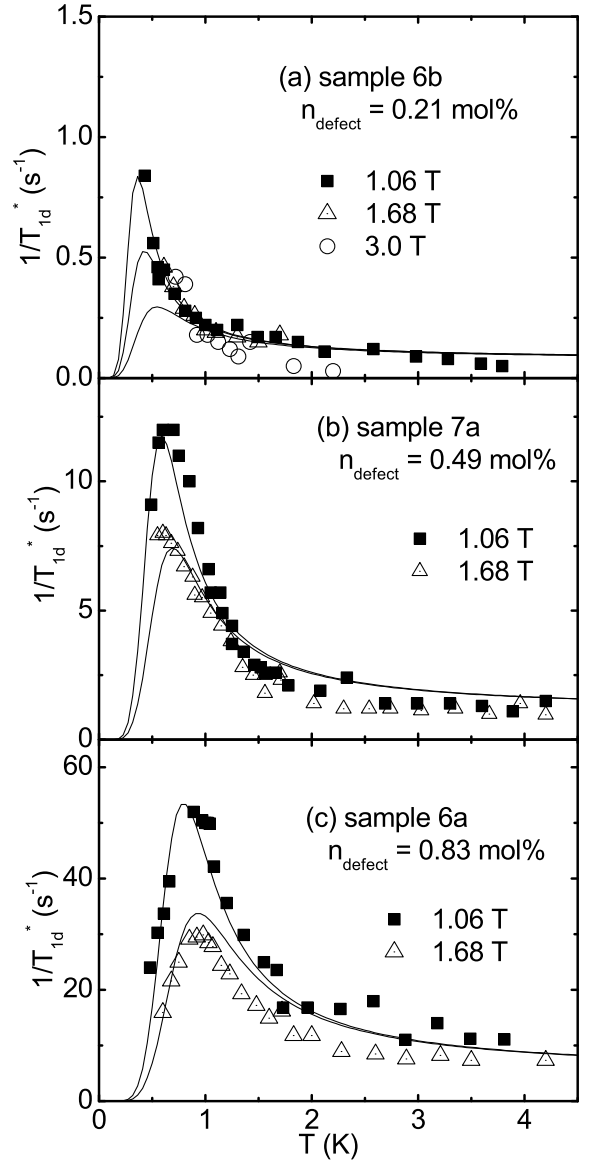


FIG. 14: $1/T_{1d}^*$ versus temperature T at applied magnetic fields $H = 1.06, 1.68,$ and 3.0 T for the LiV_2O_4 powder samples (a) 6b with $n_{\text{defect}} = 0.21$ mol%, (b) 7a with $n_{\text{defect}} = 0.49$ mol%, and (c) 6a with $n_{\text{defect}} = 0.83$ mol%. The solid curves are fits to the data by Eqs. (20) and (22).

($n_{\text{defect}} \ll 1$) that

$$p(t) = \exp \left\{ -n_{\text{defect}} \sum_i \left[1 - \exp \left(\frac{-t}{T_1(\mathbf{r}, \mathbf{x}_i)} \right) \right] \right\}. \quad (13)$$

The sum over the lattice is evaluated as an integral. In the long time limit we obtain the result $p(t)$ as given in Eq. (9) where $1/T_{1d}^*$ is then given by^{27,28}

$$\frac{1}{T_{1d}^*} = \frac{16\pi^3}{9} (\rho_N n_{\text{defect}})^2 \frac{C_0 \tau}{1 + (\omega_n \tau)^2}, \quad (14)$$

where ρ_N is the number density of LiV_2O_4 formula units.

In the Appendix, we show that instead of solving for the relaxation curve, we can understand the occurrence of a root exponential relaxation as arising from our calculated probability distribution of nuclear $1/T_1$ values. We will discuss the temperature and field dependences of $1/T_{1d}^*$ when we study the dynamics of the magnetic defects in Sec. IV B 5.

3. Hole Burning Experiment and the Dependence of Relaxation on the Position in the Spectrum

Bloembergen and coworkers²⁹ have considered the problem of spin diffusion in the frequency domain (spectral diffusion) in a spectrum with the same kind of inhomogeneous broadening as discussed for the longitudinal spin relaxation. The time for a hole to diffuse through the whole spectrum by two-spin mutual spin flip is estimated to be T_2^4/T_2^{*3} , where T_2 is the intrinsic nuclear spin-spin relaxation time and T_2^* is the half width at half maximum of the transient echo signal. In the powder sample 6a ($n_{\text{defect}} = 0.83$ mol%), $T_2 \approx 200$ μs and $T_2^* \approx 5$ μs , so $T_2^4/T_2^{*3} = 32$ s. In the powder sample 6b ($n_{\text{defect}} = 0.21$ mol%), $T_2 \approx 200$ μs and $T_2^* \approx 20$ μs which give $T_2^4/T_2^{*3} = 200$ ms. Both diffusion times are much longer than the values of T_1^* at 4.2 K in each sample in Figs. 7 and 8, and are thus consistent with the lack of spectral diffusion in Fig. 10.

The higher relaxation rates at the wings of the spectrum compared to that at the peak of the spectrum as shown in Fig. 11 can also be qualitatively explained within the approach where we only include the geometric distribution of the nuclear spin to defect separations. For concreteness of discussion, we assume that the local field is purely dipolar. Denote the angle between the applied magnetic field and the direction from a magnetic defect to a nuclear spin by θ and the distance between the defect and the nuclear spin by r . The NMR frequency shift depends on θ and r through $(1 - 3\cos^2\theta)/r^3$, while the nuclear spin-lattice relaxation rate depends on θ and r through $\sin^2\theta\cos^2\theta/r^6$.²⁰ The higher relaxation rates observed at the wings compared to that at the peak of the spectrum is due to the monotonic decrease of both the frequency shift and the nuclear spin-lattice relaxation rates with increasing distance r . The nuclear spins with larger frequency shift will also have a higher probability of having larger $1/T_1$ values.

4. ^7Li Nuclear Spin Diffusion

The $p(t)$ of powder sample 6b ($n_{\text{defect}} = 0.21$ mol%) in Fig. 12(a) deviates from a root exponential decay at $t \gtrsim 100$ ms at $T = 0.61$ K. This can be attributed to the effect of spin diffusion.³⁰ Spin diffusion tries to establish a common spin temperature (i.e., the same longitudinal magnetization) among nuclear spins at different distances from the defects and results in a single exponential relax-

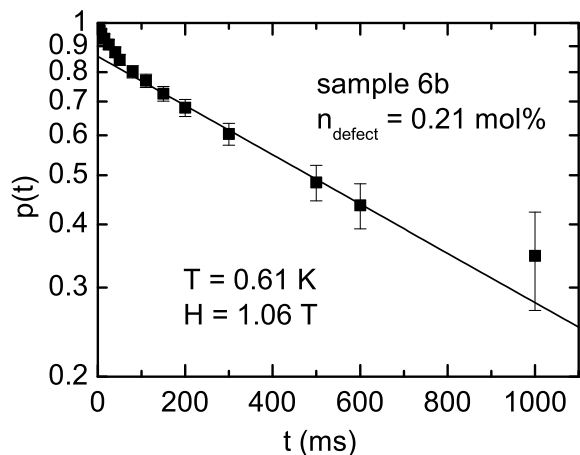


FIG. 15: Semilog plot of the nuclear spin relaxation function $p(t)$ in Eq. (8) versus time t after saturation for LiV_2O_4 powder sample 6b with $n_{\text{defect}} = 0.21$ mol% at $H = 1.06$ T and $T = 0.61$ K. The straight line is a single exponential fit to the data at $t \geq 110$ ms.

ation at long t . Figure 15 displays $p(t)$ versus t of the same data as in Fig. 12(a) at $T = 0.61$ K, but on a semilog scale, which suggests a single exponential decay at $t \gtrsim 100$ ms. A fit by $p(t) = A \exp(-t/T_1)$ to the data at $t \geq 110$ ms gives $1/T_1 = 1.1$ s^{-1} and $A = 0.86$. The best fit is shown as the straight line in Fig. 15.

A crossover from a root exponential to a single exponential decay occurs in the case of diffusion limited relaxation as discussed first by Blumberg in Ref. 30. The time t_c , at which the crossover from a root exponential to a single exponential decay takes place, is related to the spin diffusion constant D through³⁰

$$t_c = C^{1/2} D^{-3/2}, \quad (15)$$

where we dropped the subscript of C_i in Eq. (11) since we assume the same spin dynamics for all the magnetic defects. The diffusion constant D is related to the rate W of mutual flips of nearest neighbor nuclear spins through²⁰

$$D = Wa^2, \quad (16)$$

where a is the distance between the two spins. The rate of the single exponential decay at long times in Fig. 15 is given by³⁰

$$\frac{1}{T_1} = 8.5\rho_N n_{\text{defect}} C^{1/4} D^{3/4}, \quad (17)$$

where ρ_N is the number density of LiV_2O_4 formula units.

In order to confirm the spin diffusion interpretation, below we will show that the estimated crossover time t_c and $1/T_1$ are of the same order of magnitude as the observed $t_c \sim 100$ ms and $1/T_1 = 1.1$ s^{-1} , respectively. The mutual spin-flip is due to nuclear dipolar interactions and the value of W can be estimated using Fermi's golden rule. For nuclear spins having $I = 1/2$, after averaging

over the angular dependence, one obtains²⁰

$$W = \frac{2}{5}\pi \frac{\gamma_n^4 \hbar^2}{4a^6} \rho(0), \quad (18)$$

where $\rho(0)$ is the spectral density of the two spin system at zero Zeeman energy and γ_n is the gyromagnetic ratio of the nuclear spins. The ${}^7\text{Li}$ nuclei have spin $I = 3/2$, but an expression for W when $I = 3/2$ is not available, and the above equation for W should provide at least a rough estimate of W . Approximating $\rho(0)$ by $1/\sqrt{2\pi\langle\Delta\omega^2\rangle}$,²⁰ where $\langle\Delta\omega^2\rangle = 288 \text{ kHz}^2$ is the Van Vleck second moment of the ${}^7\text{Li}$ nuclei,²³ and taking $a = 3.57 \text{ \AA}$, which is the nearest-neighbor ${}^7\text{Li}$ - ${}^7\text{Li}$ distance in LiV_2O_4 , we find $W = 46 \text{ s}^{-1}$ from Eq. (18) and $D = 5.9 \times 10^{-14} \text{ cm}^2/\text{s}$ from Eq. (16).

The value of C in Eq. (15) can be obtained from Eq. (14) where $1/T_{1d}^*$ is measured using Eq. (9) from the initial root exponential part of $p(t)$ in Fig. 12(a) for powder sample 6b. At $T = 0.61 \text{ K}$ and $H = 1.06 \text{ T}$, one obtains $1/T_{1d}^* = 0.7 \text{ s}^{-1}$, so one has $C = 1.4 \times 10^{-41} \text{ cm}^6 \text{ s}^{-1}$. Using the above $D = 5.9 \times 10^{-14} \text{ cm}^2/\text{s}$ and $n_{\text{defect}} = 0.21 \text{ mol}\%$, Eq. (15) yields the crossover time $t_c = 220 \text{ ms}$ and Eq. (17) yields the long time decay rate $1/T_1 = 1.9 \text{ s}^{-1}$. Due to the uncertainty in our estimate of the parameter D and the approximate nature of Eq. (15), the estimated t_c and $1/T_1$ values should be considered to be consistent with the observed $t_c \sim 100 \text{ ms}$ and $1/T_1 = 1.1 \text{ s}^{-1}$, respectively.

The absence of a deviation from root exponential behavior in samples 7a ($n_{\text{defect}} = 0.49 \text{ mol}\%$) and 6a ($n_{\text{defect}} = 0.83 \text{ mol}\%$) as shown in Figs. 12(b) and (c) may be due to the effect of inhomogeneous broadening, which decreases the probability of overlap of Zeeman level splittings of neighboring ${}^7\text{Li}$ nuclei and results in a decrease in the spin diffusion constant D . Furthermore, due to the higher concentrations of the defects, values of $p(t)$ at $t \gtrsim 100 \text{ ms}$ in these two samples are much smaller than in the $0.21 \text{ mol}\%$ sample, making such a deviation more difficult to observe.

5. Magnetic Defect Spin Dynamics in the Powder Samples

In this section, we discuss the relation of the nuclear spin-lattice relaxation rate to the dynamics of the magnetic defects in the powder samples. We consider the weak collision limit $h \ll H$, where h is the magnitude of the local fluctuating field at the nuclear site and H is the magnitude of the static applied field. The nuclear spin-lattice relaxation rate $1/T_1$ due to an electronic magnetic defect spin at the origin is then given by²⁰

$$\frac{1}{T_1}(\mathbf{r}) = \frac{1}{\hbar^2} \sum_{\alpha=x,y,z} A_\alpha^2(\mathbf{r}) \int_{-\infty}^{\infty} \langle S_\alpha(0)S_\alpha(t) \rangle \exp(i\omega_n t) dt, \quad (19)$$

where \mathbf{r} is the position of the nuclear spin with respect to the magnetic defect, $A_\alpha(\mathbf{r})$ is the hyperfine coupling

constant between the nuclear spin and the magnetic defect, $\omega_n = \gamma_{\text{Li}} H$ is the nuclear Larmor angular frequency, and $\langle S_\alpha(0)S_\alpha(t) \rangle$ ($\alpha = x, y, z$) are the magnetic defect spin autocorrelation functions.

As indicated in the ac susceptibility measurements, the peaks in $1/T_{1d}^*$ versus T in Fig. 14 are related to spin freezing of the magnetic defects. As a first attempt, we assume a single exponential decay for the magnetic defect spin autocorrelation functions and assume that the freezing process is due to an energy barrier so that the correlation time τ follows

$$\tau = \tau_0 \exp\left(\frac{\Delta}{T}\right), \quad (20)$$

where τ_0 is the fluctuation rate of the paramagnetic defects at high temperature and Δ is the energy barrier in temperature units. For simplicity, we will assume that all the magnetic defect spins in a sample have the same correlation time τ . For dipolar or RKKY interactions, the nuclear spin-lattice relaxation rate of a ${}^7\text{Li}$ nucleus due to a nearby defect at distance r is²⁰

$$\frac{1}{T_1}(r) = \frac{2R\mu_B^2\gamma_{\text{Li}}^2 S(S+1)}{5r^6} \frac{\tau}{1 + \omega_n^2 \tau^2}, \quad (21)$$

where the angular dependence is ignored and the prefactor is written in such a way that $R = 1$ would correspond to relaxation due solely to the fluctuating dipolar field of the longitudinal component of the magnetic defect spin. The presence of additional relaxation channels would increase the value of R . By comparing Eqs. (10), (11), and (21), one has

$$C_0 = \frac{2}{5} R \mu_B^2 \gamma_{\text{Li}}^2 S(S+1).$$

Inserting this expression for C_0 into Eq. (14), the measured characteristic relaxation rate $1/T_{1d}^*$ can be written as

$$\frac{1}{T_{1d}^*} = R \frac{32\pi^3}{45} \mu_B^2 \gamma_{\text{Li}}^2 S(S+1) \rho_N^2 n_{\text{defect}}^2 \frac{\tau}{1 + \omega_n^2 \tau^2}. \quad (22)$$

At high temperatures, τ is generally much shorter than the inverse of the nuclear Larmor frequency $1/\omega_n$. As τ increases with decreasing temperature T , a peak appears in $1/T_{1d}^*$ versus T at the temperature where $\tau = 1/\omega_n$.

We fit the $1/T_{1d}^*$ data in Fig. 14 on all three powder samples simultaneously by the combination of Eqs. (20) and (22). Possible field and temperature dependences of the parameter R are ignored in the fit. There are seven free parameters in the fit, R and Δ for each sample and τ_0 which is assumed to be sample independent. The fitting results are displayed in Fig. 14 by the solid curves. The best fit value of τ_0 is $4.1 \times 10^{-10} \text{ s}$ and the best fit values of R and Δ for each sample are listed in Table II. The energy barrier Δ increases with increasing concentration of magnetic defects, which indicates that the dynamic slowing down with decreasing temperature originates from

TABLE II: Best fit values of prefactor R and energy barrier Δ obtained by fitting the $1/T_{1d}^*$ data in Fig. 14 by a combination of Eqs. (20) and (22). In order to see the correlation between defect concentrations and R and Δ , the values of $n_{\text{defect}}\sqrt{S(S+1)}$ are also listed.

Sample	$n_{\text{defect}}\sqrt{S(S+1)}$ (mol%)	R	Δ (K)
6b	0.85	0.04(4)	1.1(1)
7a	1.9	0.17(6)	1.8(2)
6a	3.6	0.24(4)	2.5(2)

the interaction between the magnetic defects. Interaction between magnetic defects should increase with increasing concentration of the magnetic defects since the average nearest-neighbor distance decreases.

The values of R in all three samples are much less than unity, a fact which cannot be explained by the presence of other nuclear spin-lattice relaxation mechanisms since additional relaxation mechanisms would increase R . Such small values of R might be related to the spin-glass like freezing as observed in the ac magnetic susceptibility measurements. In spin glass systems, the spin autocorrelation functions are highly nonexponential,^{31,32} which reduces the spectral density of the magnetic defect spin fluctuations at ω_n as compared to the Lorentzian in Eq. (22). The reduction in spectral density thus results in a reduction in the fitted value of R in Eq. (22).

C. Effects of a Size Distribution of Magnetic Droplets

Our previous discussion demonstrated that the non-exponential time dependence of the ^7Li nuclear spin-lattice relaxation in the sample of single crystals below 1.3 K cannot be understood in terms of the interaction of the nuclear spins with separable contributions from a heavy Fermi liquid and a random distribution of point-like magnetic defects. This problem is exemplified by the unphysical $p(t)$ data at long times in Fig. 13(a) where the data move away from equilibrium rather than towards equilibrium with increasing time t . An appealing approach that refines our previous analysis is based on the hypothesis that the magnetic defects are not point-like, but are rather magnetic droplets with an average size significantly larger than an atomic size. This hypothesis is supported by the large average spins of the magnetic defects inferred above in Sec. III A and previously^{14,16} to be $S \sim 2-4$. We envision that the magnetic droplets have a variable size and spin and that the corresponding microscopic internal relaxation time τ varies with droplet size. Our arguments parallel those for the unusual spin dynamics due to statistically rare fluctuations that becomes crucial in the context of Griffiths singularities close to phase transitions.^{33,34}

In most three-dimensional systems a high tempera-

ture Curie-Weiss behavior of the susceptibility with Weiss temperature θ is indicative for magnetic ordering at a lower temperature $T \sim \theta$. However, the geometric frustration for antiferromagnetic ordering within the vanadium sublattice of the spinel structure is likely the reason why long-range antiferromagnetic order is suppressed in pure LiV_2O_4 and a heavy electron state emerges instead. Defects in the crystal structure can locally lift the frustration and easily cause magnetic order in a finite region of volume $\simeq \xi^d$ around the crystal defect where the linear size ξ is, due to the proximity to an ordered state, expected to be larger than the interatomic spacing. Here d is the dimensionality of the system. These finite regions of magnetic order are what we are calling magnetic droplets.

Fluctuations in the local tendency towards order usually lead to a probability density for the linear droplet size ξ that decreases exponentially with the volume of the droplet. In three dimensions one obtains³⁵

$$P(\xi) = \frac{3\xi^2}{\xi_0^3} \exp\left[-(\xi/\xi_0)^3\right], \quad (23)$$

where ξ_0 is the mean droplet size. It is then natural to assume that the typical internal excitation energy of a droplet decreases with increasing droplet size. These excitations can change the magnitude and/or direction of the magnetic moment of the droplet. Often the excitation energy $\varepsilon \sim \hbar/\tau$ varies with ξ according to a power law

$$\tau^{-1} = D\xi^{-\psi}, \quad (24)$$

where we have set $\hbar = 1$ and τ is the relaxation time of the excitation. The arguments of Ref. 34 yield a result $\psi = d$ for classical Heisenberg spins, where $d = 3$ for the present problem. Quantum effects can then yield deviations from this behavior and typically yield exponents ψ that are larger than the above classical result.³⁶ In some cases, such as Ising spins in a magnetic field or Heisenberg spins in a metallic host,³⁶ the quantum dynamics can lead to a droplet dynamics in three dimensions where

$$\tau^{-1} \propto e^{-\alpha(\xi/\xi_0)^3}. \quad (25)$$

Finally, in case of magnetic defects with Ising anisotropy inside a metallic host, the quantum dynamics of the defect leads to a freezing of all droplets beyond a certain size, typically of order ξ_0 (see Refs. 37 and 38).

To illustrate the effects of such droplet dynamics we concentrate first on the case Eq. (24). In the absence of a microscopic model of the droplet spin dynamics we leave ψ an open parameter of the model. We start from Eqs. (9) and (14) and write

$$p(t) = \int d\xi P(\xi) \exp\left[-\left(\frac{t}{T_1^*(\xi)}\right)^{1/2}\right], \quad (26)$$

where $T_1^*(\xi)^{-1}$ is given in Eq. (22) with τ replaced by $\tau(\xi)$. In the evaluation of this average we have two very

distinct limits. If $\omega_n \tau \ll 1$ the long time behavior of the system is dominated by small clusters since $T_1^{*-1} \propto \tau$ and slow nuclear relaxation is caused by fast droplet dynamics. In this limit, the average over droplet sizes will not cause any changes in the stretched exponential behavior as compared to our previous, purely geometric, considerations for point-like magnetic defects. The inequality $\omega_n \tau \ll 1$ is expected to be valid at higher temperatures, before a freezing or dramatic slowing down of the droplet moments sets in with decreasing temperature. This is fully consistent with our findings that we obtain $\beta = \frac{1}{2}$ in this regime. The situation changes dramatically in the limit where $\omega_n \tau \gg 1$, relevant at lower temperature, i.e. most likely for $T \lesssim 1.5$ K. Now $T_1^{*-1} \propto \tau^{-1}$ and slow nuclear relaxation is tied to slow droplet relaxation. In this regime we find

$$\frac{1}{T_1^*(\xi)} \propto \xi^{-\psi}. \quad (27)$$

In the long time limit, the average over the droplet sizes in Eq. (26) can be performed via saddle point integration and yields

$$p(t) = \exp \left[- \left(\frac{t}{T_{1,\text{droplet}}^*} \right)^\beta \right] \quad (28)$$

with

$$\beta = \frac{3}{6 + \psi}, \quad (29)$$

i.e., the additional inclusion of droplet size variations yields a stretched exponent $\beta < \frac{1}{2}$. The characteristic relaxation rate of the droplets is

$$\frac{1}{T_{1,\text{droplet}}^*} \simeq R \frac{32\pi^3}{45} \frac{\mu_B^2 \gamma_{\text{Li}}^2 S(S+1) \rho_N^2 n_{\text{defect}}^2}{\omega_n^2 \tau (\xi_0)}. \quad (30)$$

We emphasize that the static size distribution of magnetic droplets only becomes apparent by NMR at low temperatures such that $\omega_n \tau > 1$, where ω_n is the nuclear Larmor frequency. We also emphasize that the analyses in this section do not include interactions between droplets and a possible resultant spin glass phase. Above $T \simeq 1.5$ K size variations of the droplets will not affect the long time nuclear relaxation, even if they are present.

In case of an exponential dependence of the droplet excitation energy, Eq. (25), the long time dynamics of the nuclear spins at low T is even more dramatically affected and changes to a power law decay $p(t) \propto t^{-\lambda}$, with nonuniversal exponent λ . At the same time heat capacity and susceptibility measurements also experience power law behavior.³⁶ In this regime droplet quantum fluctuations will not only dominate the long time dynamics of the nuclear decay, but also thermodynamics quantities. This might be responsible for the fact that it is not possible any longer to clearly separate the response of the underlying Fermi liquid from that of the droplet at

low temperatures in our single crystals, as indicated by Fig. 13(a).

Our data for single crystals do not allow at present to distinguish between the different scenarios outlined in this section. They do however suggest that dynamics of the magnetic droplets plays an important role.

V. SUMMARY AND CONCLUSIONS

The modeling approach in Sec. IV B gives a good description of our ^7Li NMR results from 0.5 to 4.2 K for our LiV_2O_4 powder samples containing magnetic defect concentrations up to 0.83 mol%. This approach assumes that (i) there is a random distribution of magnetic point defects, (ii) the heavy Fermi liquid in magnetically pure LiV_2O_4 survives in samples containing up to ~ 0.8 mol% magnetic defects, and that (iii) the influences of the magnetic defects and of the Fermi liquid on the magnetization and NMR properties are separable. This description explains very well the defect concentration-independent χ_0 value from our low-temperature magnetization measurements, the inhomogeneous broadening of the ^7Li NMR spectrum, the nonexponential ^7Li nuclear spin-lattice relaxation versus time behavior, and the lack of spectral diffusion in the ^7Li NMR hole burning experiments. It also explains the smaller ^7Li nuclear spin-lattice relaxation rate at the peak of the spectrum as compared to that at the wings. However, it is hard to reconcile the picture of magnetic point defects with the high magnetic moments for the defects (spins of 2–4) deduced here (see Table I) and in Refs. 14 and 17 from magnetization measurements. These large defect spin values suggest that the magnetic defects may not behave like point-like magnetic moments under all circumstances. In Sec. IV C we discussed magnetic defects that are more extended entities that we have called magnetic droplets with a distribution of sizes, and likely a distribution of spin values. We showed that such a size distribution can affect the NMR magnetization recovery at long times at low temperatures in the regime where interactions between the magnetic droplets can be neglected.

Our study shows that there can be different kinds of magnetic defects in the LiV_2O_4 system. As revealed by the nuclear spin lattice relaxation rate data and ac magnetic susceptibility measurements at 14 MHz, it is amazing that the magnetic defects in the powder samples undergo a spin glass-like freezing below 1 K, while the magnetic defects in the single crystals with a similar magnetic defect concentration exhibit a very different behavior at such low temperatures, with no evidence for spin freezing. The different kinds of magnetic defects and/or interactions in the crystals and powders must be associated with different types of structural defects in the system, which might be expected because the crystals are grown at about 1000 °C whereas the powders are synthesized at 700 °C. Different types of magnetic defects were even found in an annealing study of different single crystals,¹⁷

where heat treatment at 700 °C was found to remove the magnetic defects in one but not in other single crystals.

Further experiments on the single crystals are urgently needed at ~ 1 K and below. These experiments should test whether the Fermi liquid is modified by quantum fluctuations of large magnetic droplets in the single crystals at $T < 1.3$ K, whether the magnetic properties of the crystals contain separable contributions from the Fermi liquid and the magnetic defects, and whether the conduction electrons in the crystals even form a Fermi liquid. In addition, the origin of the distinct kinks at about 1.4 K in the temperature dependences of $1/T_1^*$ and β in Fig. 7 and of $M(\infty)T$ in Fig. 8 for the single crystals remains to be explained.

Acknowledgments

We are grateful to B. J. Suh for many beneficial suggestions. Work at the Ames Laboratory was supported by the Department of Energy-Basic Energy Sciences under Contract No. DE-AC02-07CH11358.

APPENDIX: PROBABILITY DISTRIBUTION UNDERLYING STRETCHED EXPONENTIAL RELAXATION WITH $\beta = 1/2$

Here we discuss the stretched exponential ${}^7\text{Li}$ nuclear relaxation versus time following saturation that arises from interactions between the ${}^7\text{Li}$ nuclear spins and a low concentration of magnetic defect spins, which is $p(t)$ in Eq. (9). We demonstrate that instead of theoretically solving for the relaxation curve and showing that it is a stretched exponential with $\beta = 1/2$ as in Sec. IV B 2, we can understand the occurrence of this root exponential relaxation as arising from the probability distribution of nuclear $1/T_1$ values.

We assume that $p(t)$ in Eq. (9) is due to a continuous sum of exponential decays with a distribution of relaxation rates $1/T_1$. Then one can write the stretched exponential relaxation function in Eq. (9) as

$$e^{-(t/T_{1d}^*)^\beta} = \int_0^\infty P(s, \beta) e^{-st/T_{1d}^*} ds, \quad (\text{A.1})$$

where s equals $1/T_1$ normalized by $1/T_{1d}^*$, i.e., $s \equiv T_{1d}^*/T_1$, and $P(s, \beta)$ is the probability density for occurrence of s for a fixed exponent β with $0 < \beta \leq 1$. Thus the stretched exponential function is the Laplace transform of $P(s, \beta)$. Closed analytic expressions for $P(s, \beta)$ with rational values of β can be obtained from the inverse Laplace transform of the stretched exponential function, and physical interpretations of the parameters $1/T_{1d}^*$ and β have been determined.^{12,26} We show below that the probability distribution of $1/T_1$ due to dipolar interaction of nuclear spins with dilute magnetic defects corresponds very well to the $1/T_1$ distribution leading to the

stretched exponential relaxation in Eqs. (9) and (A.1) with $\beta = 1/2$. This probability density is^{12,26}

$$P(s, 1/2) = \frac{e^{-\frac{1}{4s}}}{\sqrt{4\pi s^3/2}}. \quad (\text{A.2})$$

A plot of this distribution function is given below as the solid curve in Fig. 16. $P(s, 1/2)$ is proportional to $s^{-3/2}$ for large s [in general $P(s, \beta)$ at large s is proportional to $s^{-(1+\beta)}$], and has a low- s cutoff since $e^{-1/4s}$ exponentially approaches zero at small s values (also true in general for arbitrary β).²⁶

A qualitative $s^{-3/2}$ dependence of the $1/T_1$ probability distribution arises due to a r^{-6} dependence of $1/T_1$ as in Eq. (10) as follows. Ignoring the angular dependence in Eq. (10) and assuming the same dynamics for all the magnetic defect spins such that $C_l = C$, in the single paramagnetic center limit the distribution of s arising from a *continuum* distribution of nuclear spins around a magnetic defect is¹²

$$P_{\text{geo}}(s) \propto r^2 \left. \frac{dr}{ds} \right|_{r=(\frac{CT_{1d}^*}{s})^{1/6}} \propto s^{-3/2}. \quad (\text{A.3})$$

This s dependence is the same as the large- s limit of the result in Eq. (A.2) for stretching exponent $\beta = 1/2$ noted above. The distribution (A.3) diverges as $1/T_1$ approaches zero. This divergence is caused by the single impurity approximation. Nuclei with $1/T_1$ approaching zero correspond to those far away from the paramagnetic center. Due to the finite distance between different paramagnetic centers in a system with a finite concentration of them, the actual probability of finding a nuclear spin with $1/T_1 \rightarrow 0$ should instead vanish, so a low $1/T_1$ cutoff has to be applied. This results in a distribution function with a shape (see the dashed curve in Fig. 16 below) roughly similar to that in Eq. (A.2) (the solid curve in Fig. 16 below).

We have carried out a numerical simulation of the $1/T_1$ probability distribution that turns out to be in very good agreement with the exact result for the probability distribution in Eq. (A.2) for the stretched exponential function with $\beta = 1/2$. In the simulation, we calculated the $1/T_1$ distribution of ${}^7\text{Li}$ nuclei due to a random distribution of dilute point-like paramagnetic centers (defects) in the LiV_2O_4 spinel structure. The paramagnetic defects randomly occupy the vanadium sites with a probability of 0.25% ($n_{\text{defect}} = 0.5$ mol%) and the configuration of the random defects repeats every 80 unit cells in all three crystallographic axis directions. The $1/T_1$ of each ${}^7\text{Li}$ nucleus is calculated using²⁰

$$\frac{1}{T_1} = C \sum_i \frac{15 \sin^2 \theta_i \cos^2 \theta_i}{2} \frac{1}{r_i^6}, \quad (\text{A.4})$$

where C is a constant, r_i is the distance between paramagnetic center i and the ${}^7\text{Li}$ nucleus, and θ_i is the angle between the applied magnetic field and the vector from paramagnetic center i to the ${}^7\text{Li}$ nucleus. The applied magnetic field was arbitrarily chosen to be along

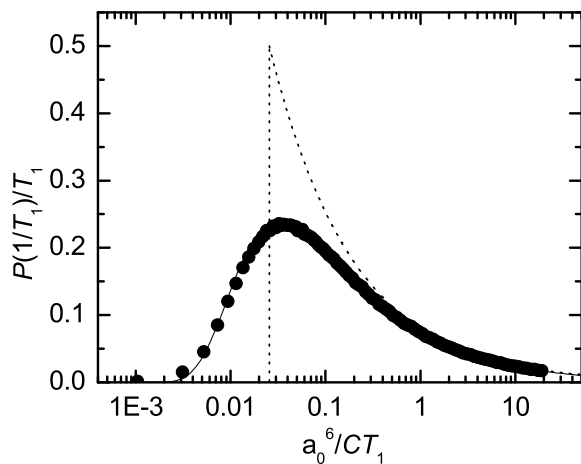


FIG. 16: ${}^7\text{Li}$ nuclear spin-lattice relaxation rate $1/T_1$ probability distributions $P(1/T_1)$, normalized by T_1 , due to dilute point-like paramagnetic defects. The filled circles are results obtained from computer simulation of LiV_2O_4 where the magnetic defects randomly occupy vanadium sites with probability 0.25%. The solid curve is the best fit of these data by Eq. (A.2) with $1/T_1^* = 0.067(1) \text{ s}^{-1}$. The dotted curve is a plot of $p(x) = 0.08x^{-3/2}$ with a small x cutoff at $x_c = 0.0256$, where $x \equiv a_0^6/CT_1$. The lower cutoff x_c is chosen so that the normalization condition $\int_{x_c}^{\infty} P(x) dx = 1$ is satisfied.

the $\langle 001 \rangle$ direction. Equation (A.4) is the nuclear spin-lattice relaxation due to the dipolar magnetic field fluctuations from the *longitudinal* spin component of the paramagnetic defects.²⁰ In the presence of a strong ap-

plied magnetic field, the *transverse* spin fluctuation is often modulated by the Larmor frequency of the *electronic* spins and thus has negligible contribution to $1/T_1$ for which magnetic field fluctuations at the *nuclear* Larmor frequency are most important.²⁰ The summation over i in Eq. (A.4) includes all magnetic defects with $r_i < 20a_0$, where $a_0 = 8.24 \text{ \AA}$ is the lattice constant of cubic LiV_2O_4 . We checked that changing the summation range to $r_i < 10a_0$ resulted in a negligible change in the $1/T_1$ distribution.

The distribution of $1/T_1$ resulting from the above simulation is displayed as the filled circles in Fig. 16, where the distribution is normalized by T_1 . The maximum relaxation rate plotted in Fig. 16 at $a_0^6/CT_1 \approx 20$ is not a large relaxation rate cutoff to the probability distribution. Data at larger relaxation rates are not plotted due to insufficient statistics. The simulated $1/T_1$ distribution in Fig. 16 can be fitted very well by Eq. (A.2) with $1/T_{1d}^* = 0.067(1)C/a_0^6$, as shown by the solid curve in Fig. 16. $1/T_{1d}^*$ calculated from Eq. (14) is equal to $0.088C/a_0^6$, close to the simulated result. The difference may be due to the neglected angular dependence in deriving Eq. (14). For comparison, a simple power law distribution $P(x \equiv a_0^6/CT_1) = 0.08x^{-3/2}$ with a small x cutoff of $x_c = 0.0256$ is also displayed in Fig. 16. This x dependence is the same as in Eq. (A.3) and is the same as the asymptotic large- s dependence of Eq. (A.2). The prefactor 0.08 is chosen to make the distribution overlap with the simulated result at large x , and the low- x cutoff $x_c = 0.0256$ is determined from the normalization condition $\int_{x_c}^{\infty} P(x) dx = 1$.

* Present address: Dipartimento di Fisica “A. Volta,” ed Unità CNISM, Università di Pavia, I-27100, Pavia, Italy

¹ S. Kondo, D. C. Johnston, C. A. Swenson, F. Borsa, A. V. Mahajan, L. L. Miller, T. Gu, A. I. Goldman, M. B. Maple, D. A. Gajewski, E. J. Freeman, N. R. Dilley, R. P. Dickey, J. Merrin, K. Kojima, G. M. Luke, Y. J. Uemura, O. Chmaissem, and J. D. Jorgensen, Phys. Rev. Lett. **78**, 3729 (1997).

² G. R. Stewart, Rev. Mod. Phys. **56**, 755 (1984).

³ H. Takagi, C. Urano, S. Kondo, M. Nohara, Y. Ueda, T. Shiraki, and T. Okubo, Mater. Sci. Eng. B **63**, 147 (1999).

⁴ C. Urano, M. Nohara, S. Kondo, F. Sakai, H. Takagi, T. Shiraki, and T. Okubo, Phys. Rev. Lett. **85**, 1052 (2000).

⁵ K. Kadowaki and W. B. Woods, Solid State Commun. **58**, 507 (1986).

⁶ P. Fulde, J. Phys.: Condens. Matter **16**, S591 (2004).

⁷ R. Arita, K. Held, A. V. Lukoyanov, and V. I. Anisimov, Phys. Rev. Lett. **98**, 166402 (2007).

⁸ V. Yushankhai, A. Yaresko, P. Fulde, and P. Thalmeier, Phys. Rev. B **76**, 085111 (2007).

⁹ A. V. Mahajan, R. Sala, E. Lee, F. Borsa, S. Kondo, and D. C. Johnston, Phys. Rev. B **57**, 8890 (1998).

¹⁰ D. C. Johnston, J. Low Temp. Phys. **25**, 145 (1976).

¹¹ M. Dalton, D. P. Tunstall, J. Todd, S. Arumugam, and P. Edwards, J. Phys.: Condens. Matter **6**, 8859 (1994).

¹² D. C. Johnston, S.-H. Baek, X. Zong, F. Borsa, J. Schmalian, and S. Kondo, Phys. Rev. Lett. **95**, 176408 (2005).

¹³ H. Kaps, M. Brando, W. Trinkl, N. Büttgen, A. Loidl, E.-W. Scheidt, M. Klemm, and S. Horn, J. Phys.: Condens. Matter **13**, 8497 (2001).

¹⁴ S. Kondo, D. C. Johnston, and L. L. Miller, Phys. Rev. B **59**, 2609 (1999).

¹⁵ M. D. Vannette, A. Safa-Sefat, S. Jia, S. A. Law, G. Laperot, S. L. Bud’ko, P. C. Canfield, J. Schmalian, and R. Prozorov, J. Mag. Mag. Mater. **320**, 354 (2007).

¹⁶ S. Das, X. Ma, X. Zong, A. Niazi, and D. C. Johnston, Phys. Rev. B **74**, 184417 (2006).

¹⁷ S. Das, X. Zong, A. Niazi, A. Ellern, J. Q. Yan, and D. C. Johnston, Phys. Rev. B **76**, 054418 (2007).

¹⁸ D. Corson and P. Lorrain, *Introduction to Electromagnetic Fields and Waves* (W. H. Freeman and Company, San Francisco, 1962).

¹⁹ E. Fukushima and S. B. W. Roeder, *Experimental Pulse NMR: A Nuts and Bolts Approach* (Perseus Books, Cambridge, 1981).

²⁰ A. Abragam, *Principles of Nuclear Magnetism* (Oxford University Press, Oxford, 1982).

²¹ J. H. Van Vleck, Phys. Rev. **74**, 1168 (1948).

²² L. E. Drain, Proc. Phys. Soc. London **80**, 1380 (1962).

- ²³ M. Onoda, H. Imai, Y. Amako, and H. Nagasawa, Phys. Rev. B **56**, 3760 (1997).
- ²⁴ C. P. Slichter, *Principles of Magnetic Resonance* (Springer, Berlin, 1990), 3rd ed.
- ²⁵ R. E. Walstedt and L. R. Walker, Phys. Rev. B **9**, 4857 (1974).
- ²⁶ D. C. Johnston, Phys. Rev. B **74**, 184430 (2006).
- ²⁷ M. R. McHenry, B. G. Silbernagel, and J. H. Wernick, Phys. Rev. B **5**, 2958 (1972).
- ²⁸ D. Tse and S. R. Hartmann, Phys. Rev. Lett. **21**, 511 (1968).
- ²⁹ N. Bloembergen, S. Shapiro, P. S. Pershan, and J. O. Artman, Phys. Rev. **114**, 445 (1959).
- ³⁰ W. E. Blumberg, Phys. Rev. **119**, 79 (1960).
- ³¹ A. T. Ogielski, Phys. Rev. B **32**, 7384 (1985).
- ³² A. P. Murani, J. Magn. Magn. Mater. **22**, 271 (1981).
- ³³ R. B. Griffiths, Phys. Rev. Lett. **23**, 17 (1969).
- ³⁴ A. J. Bray, Phys. Rev. Lett. **59**, 586 (1987).
- ³⁵ M. J. Thill and D. A. Huse, Physica A **214**, 321 (1995).
- ³⁶ T. Vojta and J. Schmalian, Phys. Rev. B **72**, 045438 (2005).
- ³⁷ A. J. Millis, D. K. Morr, and J. Schmalian, Phys. Rev. Lett. **87**, 167202 (2001).
- ³⁸ A. J. Millis, D. K. Morr, and J. Schmalian, Europhys. Lett. **72**, 1052 (2005).